

Ensemble-based estimates of the predictability of wind-driven coastal ocean flow over topography

SANGIL KIM*

COLLEGE OF OCEANIC AND ATMOSPHERIC SCIENCES
OREGON STATE UNIVERSITY, CORVALLIS, OR 97331 U.S.A.

R. M. SAMELSON

COLLEGE OF OCEANIC AND ATMOSPHERIC SCIENCES
OREGON STATE UNIVERSITY, CORVALLIS, OR 97331 U.S.A.

CHRIS SNYDER

NATIONAL CENTER FOR ATMOSPHERIC RESEARCH
P.O. Box 3000, BOULDER, CO 80307 U.S.A.

*Corresponding author address: College of Oceanic and Atmospheric Sciences, Oregon State University,
Corvallis, OR 97331 U.S.A.
E-mail: skim@coas.oregonstate.edu

Report Documentation Page			Form Approved OMB No. 0704-0188	
<p>Public reporting burden for the collection of information is estimated to average 1 hour per response, including the time for reviewing instructions, searching existing data sources, gathering and maintaining the data needed, and completing and reviewing the collection of information. Send comments regarding this burden estimate or any other aspect of this collection of information, including suggestions for reducing this burden, to Washington Headquarters Services, Directorate for Information Operations and Reports, 1215 Jefferson Davis Highway, Suite 1204, Arlington VA 22202-4302. Respondents should be aware that notwithstanding any other provision of law, no person shall be subject to a penalty for failing to comply with a collection of information if it does not display a currently valid OMB control number.</p>				
1. REPORT DATE 2008	2. REPORT TYPE	3. DATES COVERED 00-00-2008 to 00-00-2008		
4. TITLE AND SUBTITLE Ensemble-based estimates of the predictability of wind-driven coastal ocean flow over topography			5a. CONTRACT NUMBER	
			5b. GRANT NUMBER	
			5c. PROGRAM ELEMENT NUMBER	
6. AUTHOR(S)			5d. PROJECT NUMBER	
			5e. TASK NUMBER	
			5f. WORK UNIT NUMBER	
7. PERFORMING ORGANIZATION NAME(S) AND ADDRESS(ES) Oregon State University, College of Oceanic and Atmospheric Sciences, Corvallis, OR, 97331			8. PERFORMING ORGANIZATION REPORT NUMBER	
9. SPONSORING/MONITORING AGENCY NAME(S) AND ADDRESS(ES)			10. SPONSOR/MONITOR'S ACRONYM(S)	
			11. SPONSOR/MONITOR'S REPORT NUMBER(S)	
12. DISTRIBUTION/AVAILABILITY STATEMENT Approved for public release; distribution unlimited				
13. SUPPLEMENTARY NOTES Monthly Weather Review, 137, 2515-2537				
14. ABSTRACT see report				
15. SUBJECT TERMS				
16. SECURITY CLASSIFICATION OF: a. REPORT b. ABSTRACT c. THIS PAGE unclassified unclassified unclassified			17. LIMITATION OF ABSTRACT Same as Report (SAR)	18. NUMBER OF PAGES 65
19a. NAME OF RESPONSIBLE PERSON				

ABSTRACT

The predictability of coastal ocean circulation over the central Oregon shelf, a region of strong wind-driven currents and variable topography, is studied using ensembles of 50-day primitive-equation ocean model simulations with realistic topography, simplified lateral boundary conditions, and forcing from both idealized and observed wind time-series representative of the summer upwelling season. The main focus is on the balance, relevant to practical predictability, between deterministic response to known or well-predicted forcing, uncertainty in initial conditions, and sensitivity to instabilities and topographic interactions. Large ensemble and single-simulation variances are found downstream of topographic features, associated with transitions between along-isobath and cross-isobath flow, which are in turn related both to the time-integrated amplitude of upwelling-favorable wind-forcing and to the formation of small-scale eddies. Simulated predictability experiments are conducted and model forecasts are verified by standard statistics including anomaly correlation coefficient, and root mean squared error. A new variant of relative entropy, the forecast relative entropy, is introduced to quantify the predictive information content in the forecast ensemble, relative to the initial ensemble. The results suggest that, even under conditions of relatively weak wind forcing, the deterministic response is stronger than instability growth over the 3-7 day forecast intervals considered here. Consequently, important elements of the coastal circulation should be accessible to predictive, dynamical forecasts on the nominal 7-day predictability timescale of the atmospheric forcing, provided that sufficiently accurate initializations are

available. These results on predictability are consistent with inferences drawn from recent modeling studies of coastal ocean circulation along the central Oregon shelf, and should have general validity for other, similar regions.

1. Introduction

Over the last decade, numerical simulations of coastal ocean flows have begun to provide credible representations of three-dimensional, wind-forced, continental shelf circulation on horizontal scales of several to several hundred kilometers. On the central Oregon shelf, for example, primitive-equation ocean models have been shown to yield useful comparisons with in-situ and remote-sensing observations, and have been used to obtain new insights into the structure and dynamics of wind-driven circulation over the complex bathymetry of the Heceta Bank region (Oke et al. 2002a,c; Kurapov et al. 2005a).

At the same time, advances in satellite observing systems and mesoscale atmospheric modeling have greatly improved both our understanding of coastal wind fields and our ability to simulate and predict their structure. In addition, new observing technologies with real-time data reporting, such as autonomous underwater vehicles, land-based radars, and data-transmitting moorings, have been developed, which promise in the near future to provide the regular availability of synoptic data describing coastal ocean conditions on a regional scale. Thus, a practical opportunity is arising to combine these elements - numerical ocean models, coastal wind fields from operational weather forecast models, and real-time data from coastal ocean observing systems - into operational ocean prediction systems for the continental shelf.

The potential success and value of such systems will depend fundamentally on the intrinsic predictability properties of the coastal ocean. Thus far, however, these properties have received little direct attention, and been subject to little quantitative analysis. While it has long been known that a large fraction of some components of shelf flows, such as

coastal sea level and depth-integrated alongshore currents, can be understood as a linear, deterministic response to wind forcing (Battisti and Hickey 1984; Halliwell and Allen 1984), evidence for the importance of eddy processes has also existed (Bryden et al. 1980). Recent numerical studies, extending previous linear analyses such as that of Barth (1989b) and McCreary et al. (1991) have explored the nonlinear evolution of instabilities on coastal upwelling fronts and the finite-amplitude flow structures that can result (Durski and Allen 2005; Durski et al. 2007). Presumably, the presence of these instabilities will lead to disturbance and error growth dynamics that limit the skill of coastal ocean predictability in the same way that baroclinic instability and related processes in the mid-latitude atmosphere impose predictability limits on numerical weather prediction.

In the atmosphere, the literature on predictability of synoptic-scale flow for global models is vast. Perhaps more relevant by analogy to the problem of regional ocean model predictability is the smaller literature on mesoscale atmospheric predictability (Anthes et al. 1985; Errico and Baumhefner 1987; Vukicevic and Errico 1990; Zhang et al. 2002, 2003), which similarly involves the use of nested models with improved resolution of topography and improved representation of mesoscale physical processes. These models suggest that, in the atmospheric case, errors in initial and lateral boundary conditions may often limit mesoscale predictability, but, if convective or other similar processes are involved, small-scale instabilities can also play a role. There is a substantial amount of work on predictability of the coupled ocean-atmosphere ENSO phenomenon (Chen et al. 1995; Moore and Kleeman 1996), but otherwise the predictability of ocean circulation remains relatively unexplored, with a few exceptions, such as the studies by Moore and Mariano (1999) and Moore (1999) of error growth in models of the baroclinically unstable Gulf Stream jet.

In the following, a primitive-equation ocean model with realistic bathymetry is used to explore the balance, relevant to practical predictability of the coastal circulation, between deterministic response to known or well-predicted forcing, uncertainty in initial conditions, and sensitivity to instabilities and topographic interactions. The general object is to begin to develop quantitative characterizations of the intrinsic predictability of wind-driven coastal ocean flows, and of the processes that control or affect that predictability. The specific focus is on the wind-driven coastal flow over topography representing the central Oregon shelf, which is dominated by Heceta Bank, an elongated submarine ridge oriented roughly northeast to southwest across the shelf. Section 2 describes the model and its implementation in a domain representing the Oregon coastal zone. In section 3, the basic physical characteristics of the circulation in the simulations is described. The ensemble-based predictability results are discussed in section 4, along with a new variation of the relative entropy statistic. A discussion and summary are given in section 5.

2. Model formulation

For this study, a primitive-equation ocean circulation model with a terrain-following vertical coordinate (Shchepetkin and McWilliams 2003, 2005) was configured for the Oregon continental shelf and slope region (Fig. 1). The model configuration is similar to those in Oke et al. (2002a,b,c) and (Kurapov et al. 2005a,b). The model adopts the Mellor-Yamada level 2.5 turbulent closure scheme for the vertical mixing (Mellor and Yamada 1982), and Laplacian mixing along coordinate surfaces with horizontal viscosity and diffusivity equal to $2 \text{ m}^2 \text{ s}^{-1}$. The bottom stress is calculated with a quadratic drag using a bottom roughness of

$3 \cdot 10^{-3}$ m. The grid resolution is 2 km for both Latitude (41.2°N to 46.8°N) and Longitude (-127°W to -123°W), with 120 and 312 grid points in the offshore and alongshore direction, respectively, while in the vertical 31 sigma levels are used, with finest resolution near the surface and bottom with $h_c = 10$ m, $\theta = 4$, and $b = 0.9$. Realistic bottom topography is used, including the Heceta Bank submarine feature near latitude 44°N (Fig. 1). The boundary conditions are periodic in the alongshore direction (northern and southern boundaries), with rigid boundaries (no-normal flow) at the coast and the artificial offshore wall (eastern and western). The bathymetry and coastline are smoothed and matched near the south and north ends of the domain. All variables are periodic along the both ends, and f-plane is used with $f = 1.013 \cdot 10^{-4}$ throughout the domain.

In previous studies, simulations with very similar model configurations have been favorably compared with detailed physical observations in the Heceta Bank region (Oke et al. 2002a,b,c; Kurapov et al. 2005a,b). These studies establish that this ocean model configuration produces a representation of the flow in this region that is sufficiently realistic to provide a rational basis for the predictability experiments considered here. However, some important features of coastal flow fields cannot be represented in this idealized domain: for example, large-scale alongshore pressure gradients cannot develop, and exchange with the deep ocean interior is prevented. To minimize any artificial boundary effects, the present study focuses on the flow in a limited, centrally located sub-domain, between latitudes 43°N and 45°N and from the coastline to longitude 125.5°W, including and surrounding the Heceta Bank feature (Fig. 1). This reduces the influence of the artificial western boundary, and limits the direct, local influence on the flow of the artificial smoothed and matched topography at the northern and southern ends of the periodic channel. However, artificial “wrap-around”

effects may still arise from the periodic boundary condition.

For the simulations considered here, the applied wind stress is spatially uniform, with temporal variations from wind stress measured during summer 2001 at the National Data Buoy Center (NDBC) buoy 46050, located 20 km west of Newport, Oregon, at 44.62°N 124.53°W (Fig. 2). Only the meridional (alongshore) component of the buoy wind stress is used; the zonal component, which is relatively small in the observed record, is set to zero. The mean alongshore wind stress is 0.0298 N m^{-2} southward. For simplicity, no surface heat flux is applied.

For the predictability experiments, a 16-member ensemble of 50-day simulations was constructed, with identical forcing but differing initial conditions. The initial conditions for the ensemble members were obtained by adding *i.i.d.* white noise with maximum amplitude 0.5°C to the temperature field of a single solution that was initialized at rest with monthly climatology for June 2004 and forced for 10 days by a spatially uniform constant southward wind stress of 0.05 Pa. The initial field for the ensemble, after the 10-day constant forcing, has cold upwelled water along the coast and an upwelling jet over the mid-shelf, qualitatively similar to but slightly weaker than the flow during the first forecast interval discussed below (e.g., Fig. 1-b). The ensemble size of 16 was motivated by the analysis of a 30-member ensemble with idealized periodic winds, which, along with subsequent analyses of subsets of the 16-member buoy wind ensemble, indicated that the 16 members would be sufficient to capture essential aspects of the variability. A second motivation for limiting the ensemble to 16 members was computational efficiency.

3. Ensemble simulations

a. Wind-forced response

The central feature of the simulations is the formation of a coastal upwelling circulation with an associated alongshore coastal jet. In response to the coastal Ekman divergence produced by the mean southward wind stress, subsurface water upwells along the coastal boundary, and the resulting pool of cold, saline, dense upwelled water fills the inner shelf along the entire domain (Figs. 1,3). The upwelled water is separated from the warm, fresh offshore water by a front with a nominal width of 20 km, which tends to lie over the outer shelf, where the bottom depth is 100 - 200 m. Associated with the front is a baroclinic, geostrophic jet, with surface meridional velocities exceeding -0.65 m/s (Fig. 4). The position of this front and jet fluctuates with time and in space, in response to wind forcing, alongshore variations in shelf topography, and internal instability processes.

The region of most intense variability is located on the southern, downstream side of the topographic feature representing Heceta Bank (Fig. 5). An isolated maximum in sea-surface height (SSH) variance is located off the southern edge of the Bank. The surface density variance reaches its maximum slightly farther offshore, and the surface vector velocity attains a maximum variance [defined as the time-mean of $(v - \bar{v})^2 + (u - \bar{u})^2$, where v and u are meridional and zonal velocities, respectively, and \bar{v} and \bar{u} are the corresponding time-averages] at the southern side of Heceta Bank. The surface current speed [where the speed $q = (u^2 + v^2)^{1/2}$] variance has a different spatial structure, with maxima at the edges of the region of large SSH variance, indicating that the maximum of the vector velocity variance is associated with changes in flow direction, rather than speed. The fluctuating flow direction

is in turn related to the passage of eddy features through the region south of the Bank.

During the first several weeks of all of the simulations, the frontal jet follows the topographic contours back toward the coast around the southern side of Heceta Bank (Fig. 6-a). Eventually, a transition occurs to a separated flow configuration, in which the jet flows directly southward off the southern side of the Bank, crossing topographic contours into deeper water (Fig. 6-b). Prior to and during the transition to separated flow, cyclonic eddies form in the frontal jet over Heceta Bank and propagate downstream, frequently merging to form a larger eddy over the outermost, southern portion of the Bank. During the transition, the onset of cross-isobath flow of the frontal jet tends to occur in conjunction with the arrival and intensification of these eddies at the southern edge of the Bank. Transitions to separated flow occur between days 25 and 30, and again between days 45 and 50, for all ensemble members (Fig. 6-c). The separated jet reattaches to the shallower topographic contours farther downstream, near latitude 43°N, just north of Cape Blanco. Smaller scale fluctuations, presumably arising from short wavelength instabilities (Fig. 1-b) of the type discussed by Barth (1989b), Durski and Allen (2005), and Durski et al. (2007), also form along the coastal upwelling front and jet, and give rise to variance maxima near the mean position of the front and jet.

Many aspects of the behavior of the wind-forced flow in the simulation are consistent with observations of coastal ocean circulation over the central Oregon shelf. A qualitatively similar flow separation has been observed, with the frontal jet crossing isobaths southward off Heceta Bank (Castelao and Barth 2005). High-frequency radar observations have revealed suggestive evidence for the presence of similar eddy features over Heceta Bank (Kosro 2005). Similar patterns of model variability have also been found previously, in analyses of model

simulations with realistic topography that focused on instabilities of the coastal upwelling jet (Durski and Allen 2005). The dynamics of the observed and modeled separation processes, including the apparent role of the eddies, are not currently understood. A more complete analysis, in this context, of the model separation dynamics is in progress and will be reported on elsewhere. The focus here is instead on direct analysis of the predictability characteristics of the modeled coastal circulation.

b. Ensemble statistics

Large temporal and ensemble averaged variances of surface density, SSH, and surface current speed are found downstream (south) of the Heceta Bank topographic feature; the spatial structure of this ensemble-averaged variability (not shown) is very similar to that of the analogous time-averaged statistics from single ensemble members (Fig. 5). The first five days of each simulation were excluded from the averaging, to allow adjustment to initial conditions, so the corresponding interval length was 45 days. The upwelling front and southward-flowing geostrophically balanced coastal jet, and the dense (relatively cold and saline) upwelled water along the coastal boundary, are clearly evident in the ensemble mean. The mean cross-front differences in surface density, and SSH were roughly 2 kg m^{-3} , and 0.15 m , and maximum speeds in the mean jet exceed 0.5 m s^{-1} . Maximum standard deviations in these regions reach 0.6 kg m^{-3} , and 0.05 m , and 0.25 m s^{-1} .

Two different dimensionless root-mean-square norms are used here to compute the standard deviation of ensemble spread and, below, the differences between individual solutions

over the sub-domain (Fig. 1). The first, $N_3(t)$, is based on the full three-dimensional fields:

$$N_3 = V_3^{1/2}, \quad V_3 = \frac{1}{2} \left[\frac{\overline{\rho'^2}^{xyz}}{E_3(\rho'^2)} + \frac{\overline{u'^2 + v'^2}^{xyz}}{E_3(u'^2 + v'^2)} \right]. \quad (1)$$

Here $\rho'(\mathbf{x}, t) = \rho(\mathbf{x}, t) - \bar{\rho}(\mathbf{x})$, $\mathbf{u}'(\mathbf{x}, t) = \mathbf{u}(\mathbf{x}, t) - \bar{\mathbf{u}}(\mathbf{x})$, with $\bar{\rho}$, and $\bar{\mathbf{u}}$ representing ensemble- and time-averaged mean density and horizontal vector velocity fields, respectively, $\mathbf{x} = (x, y, z)$, and $(u', v') = \mathbf{u}'$. In (1), the notation $(\cdot)^{xyz}$ denotes a volume average, and $E_3(A)$ indicates the ensemble-, time-, and volume-average of quantity A . The second norm, $N_2(t)$, is based only on surface variables:

$$N_2 = V_2^{1/2}, \quad V_2 = \frac{1}{3} \left[\frac{\overline{\zeta'^2}^{xy}}{E_2(\zeta'^2)} + \frac{\overline{\rho_s'^2}^{xy}}{E_2(\rho_s'^2)} + \frac{\overline{u_s'^2 + v_s'^2}^{xy}}{E_2(u_s'^2 + v_s'^2)} \right]. \quad (2)$$

Here ζ , ρ_s , and $[u_s, v_s] = \mathbf{u}_s$ are the SSH, surface density, and surface horizontal velocity, respectively, and the decomposition into mean and fluctuations is as in (1). In (2), the notation $(\cdot)^{xy}$ denotes an area average, and $E_2(A)$ indicates the ensemble-, time-, and area-average of quantity A . The volume-averaged quantities in N_3 yield a relatively complete estimate of differences between the fields, while the surface variables in N_2 are of special interest for many potential practical uses, such as SST prediction for meteorological forecasting or surface current prediction for search and rescue operations. Although other choices of norms would, of course, lead to slightly different results, the present results are unlikely to change for any norm that is sensitive to the dominant features of the flow.

The ensemble spread N_3^{ens} for the N_3 norm is computed according to

$$N_3^{ens} = \left(\frac{1}{J} \sum_j V_{3j} \right)^{1/2}, \quad (3)$$

where the sum is over the J ensemble members ($J = 16$) and V_{3j} is the quantity V_3 in (1) computed for the difference of the j -th solution \mathbf{Y}_j from the full ensemble mean fields \mathbf{Y}_m^{ens} ,

where

$$\mathbf{Y}_m^{ens}(x, y, z, t) = \frac{1}{J} \sum_j \mathbf{Y}_j(x, y, z, t). \quad (4)$$

The computation for the ensemble spread N_2^{ens} in the N_2 norm is analogous such that

$$N_2^{ens} = \left(\frac{1}{J} \sum_j V_{2j} \right)^{1/2}, \quad (5)$$

where V_{2j} is the quantity V_2 in (2).

For the full ensembles of simulations, the quantities N_3^{ens} and N_2^{ens} grow slowly over most of the simulation interval, with final values of the corresponding norms less than twice their minimum values (Fig 8). The initial decrease, during Days 5-10, is associated with adjustment of the random initial perturbations, in which the damping of most of the initial perturbation variance exceeds the growth of jet-scale instabilities. There is some indication of more rapid growth toward the end of the period, but little suggestion overall of the sustained exponential growth that would characterize an ensemble of linearly unstable disturbance fields. On the other hand, the slow but persistent increase in ensemble variance N_3^{ens} throughout the period is also different than would be expected for linear instabilities that have equilibrated at a (statistically) steady finite amplitude, for which the ensemble variance should be essentially constant in time. This suggests that the increasing ensemble spread may be related to the integrated wind forcing, either directly, through differing state-dependent responses to the given wind forcing, or indirectly, through episodes of instability of wind-forced jets that intermittently exceed stability thresholds when the wind-driving is sufficiently strong.

c. Dynamics

In many respects, the spatial structure of the ensemble statistics is similar to that of the corresponding time-averaged statistics for individual ensemble members (Figs. 5,9). Evidently, the alongshore structure in the variance fields is controlled by topography, and not by the initial perturbations of the ensemble members, which were random and thus would have instead resulted in an ensemble variance distribution that was uniform alongshore or along the jet axis. Similarly, the timing of the jet separation events is relatively uniform across ensemble members, and does not depend sensitively on the initial perturbations, suggesting that the separation is largely a deterministic response of the wind-driven flow over topography, despite the apparent role of nonlinear eddy formation in the separation process.

However, it is not straightforward to disentangle completely the different processes that may contribute to the growth of the ensemble variance (Fig 8). The spatial structure of the ensemble variance is different for different variables and at different times during the simulation interval (Fig. 9). For SSH, the ensemble variance at fixed times is tightly concentrated in localized regions that are associated with specific large-amplitude meander or vortex features, and represent relative displacements of these features in the different ensemble members (Fig. 9-d). Surface current variability is also largest near these features, but extends more uniformly along the coastal jet (Fig. 9-e). Surface density variability is less strongly correlated with these features, and late in the simulation may be largest well offshore of the jet (Fig. 9-a,b,c).

The different degrees to which SSH, surface current, and surface density variability are tied to the locations of these features can be partially rationalized, as follows. SSH, and

to a lesser extent surface currents, are surface variables whose values can be considered depth integrals of pressure and thermal wind gradients, provided that pressure gradients and geostrophic flow at depth are weak. Thus, these variables can be expected to show a directly discernable influence of the shelf topography. Surface density, however, is subject to strong advection by surface currents, is not naturally related to the depth integral of a three-dimensional property, and will tend to act more like a passive tracer. The resulting time-dependent advection process can be anticipated to lead to a decorrelation of surface density variability from the three-dimensional flow structures that dominate the SSH and surface current fields.

Rather than attempt here to analyze in detail the dynamics that control the evolution of the individual ensemble members, we focus instead on the immediate consequences of the ensemble characteristics on the predictability of the coastal flow fields. In interpreting the results of the predictability experiments discussed in the next section, it is nonetheless useful to keep in mind the following general inferences with regard to the dynamics: The initial evolution of the random perturbations is complex, consisting of damping at most of the small scales and growth at some of the larger scales, presumably associated with flow instabilities; (2) The growing disturbances apparently equilibrate at relatively small amplitude, but the different ensemble members show different timing and position of large-amplitude meanders and vortices associated with wind-driven flow over topographic features; (3) The ensemble variance generally remains associated with topographic features throughout the simulation period, rather than being uniform alongshore, as might be anticipated in the absence of topographic influences; (4) There is slow overall growth in ensemble variance during the course of the simulation interval, apparently resulting either from flow-dependent differences

in the direct response to forcing, or from intermittent episodes of instability of the wind-forced flow.

4. Ensemble-based predictability experiments

a. Approach

There are three primary competing elements that will determine the predictability of coastal ocean circulation in the regime considered here: the deterministic response to the forcing (which may itself be either well-known or uncertain), the uncertainty in initial conditions, and error growth associated with nonlinearity and instability of the flow. In this section, we analyze the ensembles of simulations described above in order to quantify the relative importance of these elements in the context of the present model. For the general predictability problem, a fourth element of likely significance is model error, which is not addressed here.

In the standard ensemble forecast approach, a new ensemble is constructed at each initialization time, using information from the previous forecast cycle. In the present case, a simple empirical approach is used instead to construct simulated ensembles for different initialization times from the two ensembles of long-term simulations described above. The predictability experiments are constructed from the simulation ensembles as follows. For a specific choice of initial time t_0 , such as $t_0 = 24$ days, the ‘true’ solution $\mathbf{X}(t; t_0)$ is defined as the single ensemble member that is closest to the ensemble mean at the initial time $t = t_0$, with respect to a specific norm. For this true solution $\mathbf{X}(t; t_0)$, with initial time t_0 , a sim-

ulated forecast ensemble is then constructed from the remaining members of the long-term simulation ensemble. The predictability of the true solution is examined by analyzing the evolution of the forecast ensemble and the differences between the forecast ensemble members and the true solution at various forecast times. This procedure is then repeated for a new initial time t'_0 , for which a new true solution $\mathbf{X}(t; t'_0)$ is chosen in the same way from the full ensemble at $t = t'_0$. These predictability experiments are all conducted in a pure forecast setting, in which no data from the true solution is used to guide the predictive solutions.

By construction, the mean of the simulated forecast ensemble will, for each t_0 , initially be relatively close to the true solution $\mathbf{X}(t; t_0)$. As the members of the ensemble of long-term simulations diverge over time, the initial variance of the corresponding simulated forecast ensembles for successively larger values of t_0 will grow. In general, for sufficiently large t_0 , this empirical construction may not yield a useful simulated forecast ensemble, because the ensemble members may be too widely spread. Nonetheless, it is shown below that useful simulated forecast solutions, with error substantially smaller than a persistence forecast, can be obtained from the ensemble throughout the entire simulation interval.

Four different forecast quantities are considered here: climatology \mathbf{Y}_0 , persistence \mathbf{Y}_p , control \mathbf{Y}_c , and ensemble mean \mathbf{Y}_m . Of these, all but the climatology, which is constant, depend on the initialization time t_0 , while only the control and ensemble mean depend on the forecast time t . The climatology \mathbf{Y}_0 is simply the time and ensemble mean of the full ensemble of simulations, over the entire integration interval. Persistence forecast \mathbf{Y}_p is the simplest forecast that can be made, given approximate, or exact, knowledge of the initial state of a system: for a forecast from initial time t_0 , the forecast state $\mathbf{Y}_p(t; t_0)$ at time $t \geq t_0$ is presumed to be the same as the initial state $\mathbf{Y}_p(t_0; t_0)$. For simplicity, the exact initial

state is used here for the persistence forecast, so that $\mathbf{Y}_p(t; t_0) = \mathbf{X}(t_0)$. The persistence forecast provides a basic estimate that a dynamical prediction must be able to improve upon if the utility of dynamical forecasting is to be established.

The control and ensemble mean forecasts are derived from the $J - 1$ simulated forecast ensemble members \mathbf{Y}_j , $j \in I = \{1, \dots, k - 1, k + 1, \dots, J\}$, where J is the total ensemble size ($J = 16$). Here k is the omitted index for the true solution $\mathbf{X}(t)$, which is excluded from the simulated forecast ensemble. The control forecast \mathbf{Y}_c is defined as the single ensemble member that is initially closest to the true solution $\mathbf{X}(t)$ at $t = t_0$: $\mathbf{Y}_c(t; t_0) = \mathbf{Y}_j(t)$, $j = j_c$, where j_c is the value in the index set I for which $\|\mathbf{Y}_j(t_0) - \mathbf{X}(t_0)\|$ is minimum over all possible $j \in I$. This is a natural proxy for an optimal deterministic forecast. For a given ensemble, the specific choice of the control solution $\mathbf{Y}_c(t)$ depends on the definition of the norm $\|\cdot\|$ that is used to measure the initial differences.

The ensemble-mean forecast \mathbf{Y}_m is defined as the mean state at each time t of the $J - 1$ forecast ensemble members,

$$\mathbf{Y}_m(t; t_0) = \frac{1}{J - 1} \sum_{j \in I} \mathbf{Y}_j(t), \quad (6)$$

where again $I = \{1, \dots, k - 1, k + 1, \dots, J\}$, J is the total ensemble size, and k is the omitted index for the true solution $\mathbf{X}(t; t_0)$. Since the dynamical equations are nonlinear, \mathbf{Y}_m is not in general a solution of the dynamical equations, and represents instead a probabilistic forecast based on the solution ensemble.

b. Simulated forecasts

If the variability in the true solution is due primarily to a deterministic response to the wind forcing, then dynamical forecasts should yield useful predictive skill on intervals limited only by the atmospheric predictability timescale. On the other hand, if the variability is dominated by instability processes, then initial errors in the forecast fields will grow rapidly, and the dynamical forecasts will be of limited value. The relative importance of these two sources of variability and their influence on prediction accuracy are assessed here, in the context of the model simulations, by consideration of the control and ensemble-mean forecasts.

In the following predictability analysis and discussion, three choices of initial time t_0 are considered for the buoy wind case: $t_0 = \{16.5, 24, 37\}$ days. These three initialization times correspond to periods of weak-mixed upwelling and downwelling, strong upwelling, and strong-mixed winds, respectively (Figs. 2,8); the latter period includes an interval of upwelling after the strong downwelling pulse. Note that the evolution of the true solution $\mathbf{X}(t; t_0)$ during each of these intervals can be inferred by comparing the true field $\mathbf{X}(t; t_0)$ to the persistence forecast $\mathbf{Y}_p = \mathbf{X}(t_0; t_0)$: since \mathbf{Y}_p is equal to $\mathbf{X}(t; t_0)$ at time $t = t_0$, these differences of $\mathbf{X}(t; t_0)$ and \mathbf{Y}_p are equivalent to the differences between $\mathbf{X}(t; t_0)$ at time t and at time t_0 , and thus represent the evolution of the field \mathbf{X} over the interval $[t_0, t]$.

Consider first the strong upwelling period, for which $t_0 = 24$ days. For the three-day forecast from day 24, the forecast time is $t = 27$ day and the initial time $t_0 = 24$ day. Over this interval, the evolution of the true solution \mathbf{X} in the central region of interest is dominated by cyclonic rotation of the vortex of dense, upwelled water that is initially over the northern

part of Heceta Bank (Figs. 10,11). Surface density increases over southern Heceta Bank between the 200-m and 300-m isobaths, and decreases over the shallower, inshore area. The pattern of changes in SSH and surface currents follows that for surface density, and shows an oscillatory development along the upwelling front, which is centered roughly on the 250-m isobath. Differences between the true field and the persistence forecast of order $+0.8/ - 1.4 \text{ kg m}^{-3}$, $+10/ - 3 \text{ cm}$, and $+0.5/ - 0.8 \text{ m s}^{-1}$ arise in surface density, SSH, and surface current speed, respectively, over central Heceta Bank (Fig. 11).

In the strong upwelling case, both the control and the ensemble mean forecast capture the dominant evolution of the flow at day 27, the cyclonic rotation and southward movement of the vortex of dense, upwelled water over the southern side of Heceta Bank (Figs. 10,11,12). Comparison with the climatology and persistence forecast indicates that the control and ensemble mean forecasts provide quantitatively useful predictions of the evolution of the true solution from day 24 to day 27. The spatial averages on day 27 of the absolute difference from truth for the control and ensemble mean forecast fields are less than half as large as the corresponding differences for the difference of the persistence fields from truth (Table. 1). This pattern of smaller differences for the control and ensemble mean forecasts than for persistence extends throughout the 100-m depth of the water column over Heceta Bank (Fig. 12).

Similar results for 3-day forecast periods are found in the the weak-mixed and strong-mixed wind cases. In both, the dynamical forecasts generally represent well both the location and the shape of the cyclonic eddies over the Bank. The maximum differences from the truth for all forecasts are located over Heceta Bank for the weak-mixed case and southern part of the Bank for the strong-mixed case. The quantitative accuracy of the dynamical forecasts

is twice as good as persistence or climatology, and the ensemble forecasts are slightly better than the control forecasts for all surface fields. Thus, the control and ensemble forecasts, despite relatively large initial errors inherited through the long-integration ensemble method, both evidently contain useful, quantitative, predictive information on the evolution of the flow.

c. Predictability statistics

1) ROOT-MEAN-SQUARE ERRORS

Each of the three simulated forecast cases (with $t_0 = \{16.5, 24, 37\}$) involves complex flow patterns with localized, energetic variability on scales of tens of kilometers, advective modification of surface water properties, and a combination of along- and cross-isobath flow. The evolution is thus evidently nonlinear, and with its development of wave-like alongfront variability, seems likely to include instability processes. Consequently, a plausible expectation is that the evolution will be sensitive in detail to the specification of initial conditions, and that small departures from the true initial state will in each case lead to large differences in final forecast states, for the different members of the forecast ensemble.

This expectation, that the simulated forecast solutions will show rapid growth of initial error and sensitivity to initial conditions, is not met. Error growth in the dynamical forecast fields is essentially negligible, with no evident tendency toward exponential growth: the root-mean-square error (RMSE) for these forecasts remains nearly constant over each of the three forecast intervals (Fig. 13). In contrast, in all cases examined here, the error, relative to the true solution, of the persistence forecasts grows rapidly, with the persistence RMSE rapidly

exceeding twice the control and ensemble-mean RMSE for the first two forecast intervals (Fig. 13), and the N_3 and N_2 norms of the difference fields $\mathbf{Y}_p(t) - \mathbf{X}(t)$ reaching values of 0.8 or greater within 1-2 days (Fig. 14). This rapid growth of the persistence RMSE, to values substantially larger than the control and ensemble-mean RMSE within 1-2 days, is an essential result of the analysis. It illustrates that the dynamical forecasts are able to capture significant portions of the flow evolution, despite the errors inherited from the imperfect representation of the initial state.

Similarly, there are only limited changes in the spread N_3^{ens} of the full simulated forecast ensemble over the forecast interval (Fig. 14). Some growth in surface density ensemble variance occurs along the southern edge of the upwelled pool, where initial surface density ensemble variance is also concentrated. However, the amplitude and spatial scale of this variance is significantly smaller than that of the changes associated with the evolution of the true field over the three-day period. The SSH and surface current speed show even less tendency toward amplification of initial ensemble variance. Figure 14 also shows that a forecast of climatology possess errors much larger than either the ensemble spread of the error of the control or ensemble-mean forecasts. In more familiar dynamical systems such as that of Lorenz (1963) , in contrast, small differences between solutions grow until their squared difference is comparable to twice the climatological variance of the system. (This is the upper bound on the error of the persistence forecast as well.) Thus, the lack of growth in ensemble spread occurs despite the fact that the spread is substantially smaller than the climatological standard deviation, a situation in which solutions in other dynamical system continue to diverge.

The individual components of the N_3 norm, the root-mean-square errors, behave in a

qualitatively similar fashion, but with some differences between terms (Figs. 13). In all cases, the dynamical forecasts beat persistence after 1 day. The relative margin of difference, measured in terms of the ratios of the respective components, in density is comparable to that of vector velocity (Fig. 13) and SSH (not shown). The volume-averaged RMSE for the control and ensemble-mean forecasts remains below 0.05 kg m^{-3} , and 0.05 m s^{-1} , for the full 7-day forecast interval in all forecasting periods (Fig. 13), roughly equal to the corresponding ensemble variances computed relative to the ensemble mean (Fig. 14). The dimensional RMSE magnitudes for the dynamical forecasts are mostly less than half as large as those for persistence, consistent with the corresponding N_3 values generally less than 0.6 (Fig. 14). By all of these measures, all of the value of the persistence forecasts, relative to the climatology, has been lost after only 1-2 days.

2) ANOMALY CORRELATIONS

A similarly rapid decline is found in the values of the anomaly correlation coefficient C_{ac} for the persistence forecast (Fig. 15). The C_{ac} , defined as

$$C_{ac} = \frac{\overline{Cov(\mathbf{Y} - \mathbf{M}, \mathbf{X} - \mathbf{M})}}{\sqrt{\overline{Var(\mathbf{Y} - \mathbf{M})} \cdot \overline{Var(\mathbf{X} - \mathbf{M})}}}. \quad (7)$$

is the volume-averaged correlation between the difference $\mathbf{Y} - \mathbf{M}$ of the forecast \mathbf{Y} and climatological mean \mathbf{M} (Fig. 7), and the difference $\mathbf{X} - \mathbf{M}$ of the truth \mathbf{X} and \mathbf{M} ; here the correlation is the covariance of these quantities normalized by the square roots of the corresponding variances. It is widely used to assess forecast skill in numerical weather prediction (Miyakoda et al. 1986; Tracton et al. 1989; Palmer et al. 1990), for which experience suggests that forecasts with $C_{ac} < 0.6$ provide no useful guidance (e.g., Krishnamurti et al. (2003)

and references therein).

In the present case, the values C_{ac} of the persistence forecasts for the density and vector velocity all drop below 0.6 within 1-2 days (Fig. 15). Thus, the persistence forecasts of the structure of the anomaly fields, relative to the corresponding climatological means, also retain little value after only 1-2 days. The values of C_{ac} for the dynamical forecasts are generally larger than 0.6, and generally similar for both wind cases for all fields, except for vector velocity of the control forecast for $t_0 = 37$ days, which declines below 0.6. This pattern is consistent with that for N_3 and the RMSE, such that the dynamical forecasts show robust predictability even during the interval in which the transition to separated flow occurs.

In all cases examined here, and by all three measures introduced above (the N_3 norm, RMSE, and C_{ac}), the control and the ensemble-mean forecasts are more accurate than persistence for all forecast intervals between 1 and 7 days. For $t_0 = \{16.5, 24, 37\}$ days, for example, the difference norm $\|\mathbf{Y}_{c,m}(t) - \mathbf{X}(t)\|_{N_3}$ of control or ensemble-mean and truth have values less than half as large as the corresponding difference norms for persistence and truth (Fig. 14). The improvement in accuracy is found despite the systematically larger initial errors of the control and ensemble-mean forecasts, relative to persistence. This basic comparison illustrates the potential predictive value of dynamical forecasting in the coastal ocean. It appears to derive primarily from the strong response of the coastal ocean to the imposed wind-stress forcing; note, however, that the dynamical forecasts are also successful during the first forecast interval, which has only weak wind forcing (Table 1).

During the weak-mixed and strong upwelling wind periods, N_3 difference norms for both the control and ensemble mean forecasts do not change much, but during the strong-mixed wind period, the norm for the control appear to increase more significantly (Fig. 14). The

initial errors are also larger during the strong-mixed wind period, which may be partially responsible for this difference. For all three of these time intervals, the ensemble-mean forecast is comparable to, or more accurate than, the control forecast.

In these comparisons, the differences between persistence and truth continue to increase with time for forecast intervals greater than 7 days, while the error growth for the dynamical forecasts grows more slowly, which would appear to indicate the possibility of useful prediction on longer time scales. Since practical predictions of wind-forcing in coastal zones are themselves limited by uncertainty in atmospheric conditions, however, the forecast experiments considered here are generally restricted to 7 days, a rough estimate of the timescale for loss of predictive skill at mid-latitudes in current global numerical weather prediction models.

3) FORECAST RELATIVE ENTROPY

A statistical quantity known as *relative entropy* has been recently introduced in geophysical fluid dynamics to quantify predictive information content in forecast ensembles (Kleeman 2002; Abramov et al. 2005). Here, we consider a new variant of the relative entropy that we term the *forecast relative entropy*.

The relative entropy \mathcal{R} is given in information theory (Cover and Thomas 1991) by

$$\mathcal{R}(\mathbf{p}|\mathbf{q}) = \int \mathbf{p}(\mathbf{x}) \cdot \log \left[\frac{\mathbf{p}(\mathbf{x})}{\mathbf{q}(\mathbf{x})} \right] d\mathbf{x}, \quad (8)$$

where \mathbf{x} represents the state variables of the system, and \mathbf{p} and \mathbf{q} are probability distribution functions (PDFs). Thus, the dimensionless quantity \mathcal{R} is a measure of the additional information content in one PDF relative to another PDF. This is a convex, non-symmetric, and

non-negative functional in \mathbf{p} , and equal to zero only when $\mathbf{p} = \mathbf{q}$. The relative entropy also has attractive properties as a measure of predictability; for example, it is invariant under arbitrary changes of variables (Majda et al. 2002; Schneider and Griffies 1999). Moreover, when the PDFs, \mathbf{p} and \mathbf{q} , are approximately Gaussian, the numerical calculation of \mathcal{R} can be simplified into two components (Kleeman 2002; Majda et al. 2002).

In this Gaussian case, the \mathcal{R} becomes the sum of the signal \mathcal{S} and dispersion \mathcal{D} , so that $\mathcal{R} = \mathcal{S} + \mathcal{D}$, where

$$\mathcal{S} = \frac{1}{2}(\Theta_{\mathbf{p}} - \Theta_{\mathbf{q}})^{\top} \Sigma_{\mathbf{q}}^{-1} (\Theta_{\mathbf{p}} - \Theta_{\mathbf{q}}), \quad (9)$$

$$\mathcal{D} = \frac{1}{2} \left[\log \left\{ \frac{\text{Det}(\Sigma_{\mathbf{q}})}{\text{Det}(\Sigma_{\mathbf{p}})} \right\} + \text{Tr}\{\Sigma_{\mathbf{p}} \Sigma_{\mathbf{q}}^{-1}\} - n \right]. \quad (10)$$

Here $\Theta_{\{\mathbf{p}, \mathbf{q}\}}$, $\Sigma_{\{\mathbf{p}, \mathbf{q}\}}$ are the means and covariances of \mathbf{p} , \mathbf{q} , respectively, Det and Tr denote the determinant and trace of the corresponding matrices, and n is the dimension of the state space under consideration. The signal \mathcal{S} is a statistical distance, also known as the Mahalanobis distance (Mahalanobis 1936; Manly 2004), between the mean states of the PDFs. When the difference of the two mean states $\Theta_{\{\mathbf{p}, \mathbf{q}\}}$ is large relative to the covariance $\Sigma_{\mathbf{q}}$ of the PDF \mathbf{q} , the signal \mathcal{S} is large, and the two mean states are statistically different from each other. The dispersion \mathcal{D} quantifies the difference in the ensemble spreads of the two distributions, as measured by the covariances $\Sigma_{\{\mathbf{p}, \mathbf{q}\}}$ and is always a positive number unless $\Sigma_{\mathbf{p}} = \Sigma_{\mathbf{q}}$. Note that if $\Theta_{\mathbf{p}} = \Theta_{\mathbf{q}}$, then $\mathcal{S} = 0$, and if $\Sigma_{\mathbf{p}} = \Sigma_{\mathbf{q}}$, then $\mathcal{D} = 0$. If \mathbf{p} is distributed either more narrowly or more broadly than \mathbf{q} , then \mathcal{D} will be positive, as the change in the distribution \mathbf{p} represents additional predictive information content relative to the reference distribution \mathbf{q} . Note that this means that an increase in ensemble spread for \mathbf{p} relative to \mathbf{q} appears as a positive dispersion component contribution to the predictive

information content, despite the growth in uncertainty regarding the value of the state itself. In the conventional relative entropy, the distribution \mathbf{q} is usually defined in terms of a climatology such that the relative entropy monotonically decreases to zero in time, implying that the forecast \mathbf{p} converges asymptotically to the climatology \mathbf{q} .

The object of the present study is to examine the potential value of dynamical forecasts of certain coastal ocean flows, relative to the best available estimate of a given, initial estimate of the ocean state. Thus, it is natural to seek a quantitative measure of the potential value of the ensemble of dynamical forecasts, relative to the initial ensemble. In the framework of the relative entropy, such a measure can be constructed by constructing a relative entropy quantity for which $\mathbf{q}(\mathbf{x})$ represents the initial ensemble distribution (or analysis PDF) and $\mathbf{p}(\mathbf{x})$ represents the forecast ensemble distribution (or forecast PDF). We shall refer to this quantity as the *forecast relative entropy* \mathcal{R}_f . We define it here in terms of a Gaussian approximation to point-by-point PDFs,

$$\mathcal{R}_f = \overline{\mathcal{S}_f + \mathcal{D}_f}, \quad \mathcal{S}_f = \frac{1}{2} \frac{(\theta_{\mathbf{p}} - \theta_{\mathbf{q}})^2}{\sigma_{\mathbf{q}}^2}, \quad \mathcal{D}_f = \frac{1}{2} \left[\log\left\{\frac{\sigma_{\mathbf{q}}^2}{\sigma_{\mathbf{p}}^2}\right\} + \frac{\sigma_{\mathbf{p}}^2}{\sigma_{\mathbf{q}}^2} - 1 \right], \quad (11)$$

where $\theta_{\{\mathbf{p}, \mathbf{q}\}}$, $\sigma_{\{\mathbf{p}, \mathbf{q}\}}$ are respectively means and covariances of \mathbf{p} , \mathbf{q} at each grid point ($n = 1$), and $\overline{(\cdot)}$ denotes a volume average. Although the forecast relative entropy \mathcal{R}_f does not have the convenient asymptotic characteristics of the standard relative entropy, the forecast relative entropy \mathcal{R}_f does have the essential quantitative property that larger \mathcal{R}_f indicates more, and smaller \mathcal{R}_f indicates less, predictive information content in the forecast ensemble relative to the initial ensemble. Thus, it provides a direct measure of the utility of the ensemble forecast relative to the analysis.

The forecast relative entropy \mathcal{R}_f for the three simulated forecast cases discussed above,

with $t_0 = \{16.5, 24, 37\}$, shows that the predictive information content of the forecast ensemble, relative to the initial ensemble, is dominated by the signal, that is, by the difference in the means of the forecast and initial ensembles (Fig. 16). Overall, the results show that there is not much difference between the initial and the dynamical forecast ensembles during the first day of the forecast interval, but after one day \mathcal{R}_f indicates more information content in the forecast ensembles, consistent with the results of the anomaly correlation analysis. The magnitudes of the information gain vary in the three different experiments. There is more predictability during the strong upwelling wind period ($t_0 = 24$), slightly less predictability during the weak-mixed upwelling and downwelling wind period ($t_0 = 16.5$), and least predictability during the strong-mixed wind period ($t_0 = 37$).

The result that the signal component, associated with the ensemble means, of the forecast relative entropy is significantly more important than the dispersion component, associated with the ensemble spread, is consistent with the results in sections 4-b and 4-c. That is, as the forecast progresses, the larger magnitude of signal than dispersion in forecast relative entropy indicates that the directly wind-forced response and the deterministic internal dynamics are a more important factor in the evolution of the flow than internal instabilities, which would tend to spread the ensemble and increase the dispersion component. Since this is true also for the weak-mixed wind interval, quasi-deterministic dynamics of the existing wind-forced circulation and its interaction with topography must also contribute. If internal instabilities were a major contributor to the evolution, one would instead anticipate a rapid growth of ensemble variance such that the dispersion component would exceed the signal component. The result that the signal component dominates the dispersion component in the forecast relative entropy is similar to some recent results for the standard, climatology-

based relative entropy in the context of large-scale atmosphere-ocean dynamics (Kleeman et al. 2002; Kleeman and Moore 1999).

4) CROSS-SHELF VELOCITY

A traditional and still outstanding problem in coastal oceanography is the determination of the structure and dynamics of the cross-shelf circulation in coastal upwelling (Allen 1980; Brink 1991). Comparison of wind-driven circulation models with current meter mooring data has generally found that model skill in reproducing observed cross-shelf velocities is substantially lower than for along-shelf velocities (Dever 1997; Pullen and Allen 2000; ?). This issue is explored briefly here by repeating the ensemble skill measures in the previous section with an alternative norm that focuses on the cross-topography circulation.

The cross-shelf or cross-topography velocity $u_h(x, y, z, t)$ is defined here by $u_h = \mathbf{u} \cdot \mathbf{n}_h$ for all depth z , where \mathbf{u} is a velocity vector and \mathbf{n}_h is the local direction of the topographic gradient at each model grid point such that

$$\mathbf{n}_h = \frac{\nabla h(x, y)}{|\nabla h(x, y)|}.$$

The modified norm N_h is computed as the analog of the N_3 norm in (1) for u_h , and the volume-averaged statistical quantities of predictive skill described previously, RMSE, ACC and FRE are also calculated for the different forecasts such as persistence, control and ensemble-mean. For all of these quantities, the upper 20 m of the water column is excluded, so that the Ekman response to the wind forcing, which is known to be strongly predictable, does not dominate the statistics. Note that observational analyses frequently define cross-shelf as the direction of the minor-axis of the velocity variance ellipse, rather than the

intrinsically topographic definition used here.

The ensemble spread calculated using the norm N_h shows a roughly linearly increasing trend with time, as for the full norms (Fig 8), and the RMSE for the different forecasts are qualitatively the same for the cross-shelf velocity u_h and the full vector velocity in all forecasts (Figs 13, 17). The FRE and ACC also show qualitatively similar results for the vector and cross-shore velocity fields, with somewhat lower values for the cross-shore velocity ACC during the strong-mixed wind period (Figs. 15,16).

Based on these statistics, the cross-shelf velocity shows quantitative predictability that is similar to the other components of the flow. This is surprisingly large, since observational studies have suggested that the cross-shelf flow is less predictable, or at least less reproducible with existing models, than is the alongshore flow. Some of this difference may possibly arise from the different definition of the cross-shelf direction; for example, with a definition based on the observed velocity variance ellipse, persistent correlation of localized cross-shelf flow features with topography may lead to the predictable component of the true cross-shelf flow being excluded from the observationally defined cross-shelf flow. Examination of the time- and depth-averaged variance of N_h shows that the peak values are localized along the topography at the southern (where the bottom depth is 300-700 m) and northeast (where the bottom depth is 50-150 m) edges of Heceta Bank. These are areas where the topographic gradients are large.

5) ADDITIONAL SENSITIVITY ANALYSIS

The preceding discussion has shown that similar predictability results were obtained for the three different forecasting intervals, despite the different effective spin-up times, the relatively large ensemble variances, and the different wind forcing during the three intervals. This similarity suggests that the predictability results should not be overly sensitive to the initialization procedure. An additional sensitivity study was carried out in order to test this inference.

For the sensitivity study, the initial control state was taken to be the ensemble mean from the original study at Day 35, when the wind stress has a zero crossing. The corresponding initial perturbations, also obtained from the original ensemble, were the difference fields of temperature between the individual members and the ensemble mean at Day 44, the end of the third forecasting interval. The variability of the perturbations was between -1.5°C and 2°C, with high variances located around the coastal jet and having spatial scales similar to scales of the instabilities studied by Durski and Allen (2005). The new set of 16 ensemble members was then obtained by adding these perturbations, scaled down by 50%, to the control state. All members in the new set were then integrated for 13.5 days with the wind forcing from Day 10 to Day 23.5.

Statistics for the sensitivity study were computed for the last 7 days of the 13.5 day integration, which has the same wind forcing as the first (Day 16.5 through Day 23.5) forecast interval from the original ensemble. The corresponding N_3 , RMSE, ACC and FRE statistics (Fig. 18) are qualitatively similar to the previous results, with the control and ensemble-mean forecasts better than persistence after 1 day. The ensemble spread N_3^{ens}

also shows similar results: it does not show exponential growth, and instead increases until around Day 10 and then saturates.

The sensitivity study was repeated with perturbations scaled by factors 0.05 and 1. Except for the ACC of density for control forecast with perturbation factor 1, all of the results were very similar and consistent with the results reported above that were based only on the original ensemble integrations.

5. Discussion and Summary

It is well known that the coastal ocean responds strongly to wind forcing (Allen 1980; Brink 1991). That this response has a primary deterministic component is further evident from the success of linear, one-dimensional, forced-damped coastal-trapped wave models (Halliwell and Allen 1984; Chapman 1987), by which significant fractions of observed variance in alongshelf velocity and coastal sea level can be reproduced when the models are forced with observed wind stress time series. The present simulations and analysis provide evidence that this deterministic response can be translated into quantitative predictive skill of regional circulation using numerical coastal ocean circulation models with realistic bottom topography and coastline geometry. For a given initialization, this skill appears to be primarily limited by the prediction timescale of the atmospheric variability that itself determines the coastal wind fields.

In the central Oregon shelf region of interest, the dominant variability in these simulations is associated with the transition to separated flow downstream of the Heceta Bank topographic feature. This transition occurs roughly between days 25 and 30 in all of the en-

semble members, and thus appears itself to be a quasi-deterministic response to the forcing. This transition was seen more clearly in a set of simulations with time-periodic wind forcing, which were not discussed here: in those simulations, the separation was found to occur progressively earlier in simulations with successively stronger southward time-mean stress. However, the details of the separation events appear to be connected with the formation and propagation of eddies in the frontal jet over Heceta Bank, which differs among the ensemble members and evidently involves instability processes. The dynamics of the separation process remain poorly understood; an analysis of this process in the present simulations is in progress and will be reported elsewhere.

Even during the separation events, however, the role of instabilities in limiting the intrinsic predictability of the model fields appears to be relatively small. This finding would appear to be inconsistent with recent and earlier studies (Durski and Allen 2005; Barth 1989a,b) that have emphasized the importance of instabilities of coastal upwelling fronts, and explored their characteristics. Under similar conditions, however, the variability exhibited by models such as that considered by Durski and Allen (2005) is very similar to that in the present model. For example, the patterns of surface density variability in the present simulation (Figs. 3,5,7) are similar in structure to that found by Durski and Allen (2005) (their Fig. 21). The present simulations and analysis suggest that, even under conditions of relatively weak wind forcing, the deterministic response is substantially stronger than the instability growth. Consequently, important elements of the coastal circulation should be accessible to predictive, dynamical forecasts, provided that sufficiently accurate initializations and forcing fields are available. These conclusions should have general validity for similar regions of strongly wind-driven flow over large-amplitude shelf topography.

A critical element in any practical prediction scheme will, of course, be the initialization procedure, and the acquisition of sufficient initialization data. This issue has not been addressed by the present simulations and analysis. Rather, it has been implicitly assumed that the control and ensemble-mean initializations provide a reasonable representation of the accuracy at which initializations will be possible for practical schemes. Consideration of the initial N_2 and N_3 norm, and RMSE values for these solutions place the corresponding accuracy at values of one-quarter to one-half of the climatological variances. In dimensional terms, this corresponds to volume-averaged RMSE for surface density, SSH, and surface current of 0.03 kg m^{-3} , 1 cm , and 0.02 m s^{-1} , respectively. Analyses of surface and moored current observations (Kosro 2005) indicate that substantial fractions of observed variance in shelf flow fields can be captured by a relatively small number of empirical modes, suggesting that usable initializations will be possible in spite of the sparseness of anticipated observing systems, if the observing system assets are properly located. However, achieving this level of initialization accuracy within the constraints of affordable observing systems will be a significant challenge.

Acknowledgments.

The authors would like to thank the anonymous reviewers for many helpful suggestions, which greatly improved the presentation of this paper. This research was supported by the U.S. Office of Naval Research, Grant N00014-05-1-0891, through the National Ocean Partnership Program.

REFERENCES

Abramov, R., A. Majda, and R. Kleeman, 2005: Information theory and predictability for low-frequency variability. *J. Atmos. Sci.*, **62**, 65–87.

Allen, J. S., 1980: Models of wind-driven currents on the continental shelf. *Ann. Rev. Fluid Mech.*, **12**, 389–433.

Anthes, R. A., Y. H. Kuo, D. P. Baumhefner, R. P. Errico, and T. W. Bettge, 1985: Predictability of mesoscale atmospheric motions. *Adv. Geophys.*, **28**, 159–202.

Barth, J. A., 1989a: Stability of a coastal upwelling front: Part I. model development and a stability theorem. *J. Geophys. Res.*, **94**, 10 844–10 856.

Barth, J. A., 1989b: Stability of a coastal upwelling front: Part II. model results and comparison with observations. *J. Geophys. Res.*, **94**, 10 857–10 883.

Battisti, D. and B. Hickey, 1984: Application of remote wind-forced coastal trapped wave theory to the oregon and washington coasts. *J. Phys. Oceanogr.*, **14**, 887–903.

Brink, K. H., 1991: Coastal-trapped waves and wind-driven currents over the continental shelf. *Annu. Rev. Fluid Mech.*, **23**, 389–412.

Bryden, H. L., D. Halpern, and R. D. Pillsbury, 1980: Importance of eddy heat flux in a heat budget for oregon coastal waters. *J. Geophys. Res.*, **85**, C11 6649–6653.

Castelao, R. M. and J. A. Barth, 2005: Coastal ocean response to summer upwelling favorable winds in a region of alongshore bottom topography variations off oregon. *J. Geophys. Res.*, **110**, C10S04 doi:10.1029/2004JC002409.

Chapman, D. C., 1987: Application of wind-forced, long, coastal-trapped wave theory along the california coast. *J. Geophys. Res.*, **92**, 1798–1816.

Chen, D., S. E. Zebiak, A. J. Busalacchi, and M. A. Cane, 1995: An improved procedure for el nio forecasting: Implications for predictability. *Science*, **269**, 1699–1702.

Cover, T. M. and J. A. Thomas, 1991: *Elements of Information Theory*. John Wiley & Sons, 576 pp.

Dever, E., 1997: Wind-forced cross-shlef circulation on the northern california shelf. *J. Phys. Oceanogr.*, **27**, 1566–1580.

Durski, S. M. and J. S. Allen, 2005: Finite-amplitude evolution of instabilities associated with the coastal upwelling front. *J. Phys. Oceanogr.*, **35**, 1606–1628.

Durski, S. M., J. S. Allen, G. D. Egbert, and R. M. Samelson, 2007: Scale evolution of finite amplitude instabilities on a coastal upwelling front. *J. Phys. Oceanogr.*, **37**, 837–854.

Errico, R. and D. Baumhefner, 1987: Predictability experiments using a high-resolution limited-area model. *Mon. Wea. Rev.*, **115**, 488–504.

Halliwell, G. R. and J. S. Allen, 1984: Large-scale sea level response to atmospheric forcing along the west coast of north america, summer 1973. *J. Phys. Oceanogr.*, **14**, 864–886.

Kleeman, R., 2002: Measuring dynamical prediction utility using relative entropy. *J. Atmos. Sci.*, **59**, 2057–2072.

Kleeman, R., A. J. Majda, and I. Timofeyev, 2002: Quantifying predictability in a model with statistical features of the atmosphere. *Proc. Natl. Acad. Sci.*, **99**, 15 291–15 296.

Kleeman, R. and A. M. Moore, 1999: A new method for determining the reliability of dynamical ENSO predictions. *Mon. Wea. Rev.*, **127**, 694–705.

Kosro, P. M., 2005: On the spatial structure of coastal circulation off newport, oregon, during spring and summer 2001 in a region of varying shelf width. *J. Geophys. Res.*, **110**, C10S06, doi:10.1029/2004JC002769.

Krishnamurti, T. N., K. Rajendran, and T. S. V. V. Kumar, 2003: Improved skill for the anomaly correlation of geopotential heights at 500 hPa. *Mon. Wea. Rev.*, **131**, 1082–1102.

Kurapov, A. L., J. S. Allen, G. D. Egbert, and R. N. Miller, 2005a: Modeling bottom mixed layer variability on the mid-oregon shelf during summer upwelling. *J. Phys. Oceanogr.*, **35**, 1629–1649.

Kurapov, A. L., J. S. Allen, G. D. Egbert, R. N. Miller, P. R. Kosro, M. D. Levine, and T. J. Boyd, 2005b: Distant effect of assimilation of moored currents into a model of coastal wind-driven circulation off oregon. *J. Geophys. Res.*, **110**, C02022 doi:10.1029/2003JC002195.

Lorenz, E. N., 1963: Deterministic nonperiodic flow. *J. Atmos. Sci.*, **20**, 130–141.

Mahalanobis, P. C., 1936: On the generalised distance in statistics. *Proceedings of the National Institute of Science of India*, **12**, 49–55.

Majda, A., R. Kleeman, and D. Cai, 2002: A mathematical framework for quantifying predictability through relative entropy. *Methods and Application of Analysis*, **9**, 425–444.

Manly, B. F., 2004: *Multivariate Statistical Methods: A Primer, 3rd Edition*. Chapman & Hall/CRC, New York, 241 pp.

McCreary, J. P., Y. Fukamachi, and P. K. Kundu, 1991: A numerical investigation of jets and eddies near an eastern ocean boundary. *J. Geophys. Res.*, **96**, 2515–2534.

Mellor, G. L. and T. Yamada, 1982: Development of a turbulence closure model for geophysical fluid problems. *Rev. Geophys. Space Phys.*, **20**, 851–875.

Miyakoda, K., J. Sirutis, and J. Poshay, 1986: One-month forecast experiments- without anomaly boundary forcings. *Mon. Wea. Rev.*, **114**, 2363–2401.

Moore, A. M., 1999: The dynamics of error growth and predictability in a model of the gulf stream. part II: Ensemble prediction. *J. Phys. Oceanogr.*, **29**, 762–778.

Moore, A. M. and R. Kleeman, 1996: The dynamics of error growth and predictability in a coupled model of enso. *Quart. J. Roy. Meteor. Soc.*, **122**, 1405–1446.

Moore, A. M. and A. Mariano, 1999: The dynamics of error growth and predictability in a model of the gulf stream. part I: Singular vector analysis. *J. Phys. Oceanogr.*, **29**, 158176.

Oke, P. R., J. S. Allen, R. N. Miller, and G. D. Egbert, 2002a: A modeling study of the three-dimensional continental shelf circulation off oregon. part II: Dynamical balances. *J. Phys. Oceanogr.*, **32**, 1383–1403.

Oke, P. R., J. S. Allen, R. N. Miller, G. D. Egbert, and P. R. Kosro, 2002b: Assimilation of surface velocity data in to a primitive equation coastal ocean model. *J. Geophys. Res.*, **107**, 3122, doi:10.1029/2000JC000511.

Oke, P. R., et al., 2002c: A modeling study of the three-dimensional continental shelf circulation off oregon. part I: Model-data comparisons. *J. Phys. Oceanogr.*, **32**, 1360–1382.

Palmer, T. N., C. Brancovic, F. Molteni, S. Tibaldi, L. Ferranti, A. Hollingworth, U. Cubasch, and E. Klinker, 1990: The european center for medium-range weather forecasts (ECMWF) program on extended-range prediction. *Bull. Amer. Meteror. Soc.*, **71**, 1317–1330.

Pullen, J. D. and J. S. Allen, 2000: Modeling studies of the coastal circulation off northern california: shelf response to a major eel river flood event. *Contin. Shelf. Res.*, **20**, 2213–2238.

Schneider, T. and S. Griffies, 1999: A conceptual framework for predictability studies. *J. Clim.*, **12**, 3133–3155.

Shchepetkin, A. F. and J. C. McWilliams, 2003: A method for computing horizontal pressure-gradient force in an oceanic model with a nonaligned vertical coordinate. *J. Geophys. Res.*, **108**, (C3)3090 doi:10.1029/2001JC001047.

Shchepetkin, A. F. and J. C. McWilliams, 2005: The regional ocean modeling system: A split-explicit, free-surface, topography following coordinates ocean model. *Ocean Modelling.*, **9**, 347–404.

Springer, S. R., R. M. Samelson, J. S. Allen, G. D. Egbert, A. L. Kurapov, R. N. Miller, and J. C. Kindle, 2008: A nested grid model of the oregon coastal transition zone: Simulations and comparisons with observations during the 2001 upwelling season. *submitted to J.*

Geophys. Res.

Tracton, M. S., K. Mo, and W. Chen, 1989: Dynamical extended range forecasting (DERF) at the national meteorological center. *Mon. Wea. Rev.*, **117**, 129–173.

Vukicevic, T. and R. Errico, 1990: The influence of artificial and physical factors upon predictability estimates using a complex limited-area model. *Mon. Wea. Rev.*, **118**, 1460–1482.

Zhang, F. C., C. Snyder, and R. Rotunno, 2002: Mesoscale predictability of the surprise snowstorm of 2425 january 2000. *Mon. Wea. Rev.*, **130**, 16171632.

Zhang, F. C., C. Snyder, and R. Rotunno, 2003: Effects of moist convection on mesoscale predictability. *J. Atmos. Sci.*, **60**, 11731185.

List of Figures

1	Model domain vs. longitude and latitude. The inner rectangle indicates the Heceta Bank region, in which ensemble and forecast skill statistics are calculated. (a) Topographic contours (0-, 100-, 200-, 500-, 1000-, and 2000-m contours; thin solid lines; 0 m, thick solid) (b) Surface density (kg m^{-3} - 1000) at Day 16.5 for the single ensemble member #11.	45
2	Alongshore component of buoy wind stress (N m^{-2}) vs time (days). The three forecast experiment intervals are indicated (horizontal line segments).	46
3	Surface fields of the single ensemble member #11 at Day 50 vs. longitude and latitude. (a) Density (kg m^{-3} - 1000), (b) SSH (m), and (c) vector velocity and contours of speed (m s^{-1}). The 100-, 200-, 500-, 1000-, and 2000-m topographic contours are shown (thin lines).	47
4	Cross-sections vs. longitude and depth at Latitude 44.6°N from the single ensemble member #11. (a,b) Density (kg m^{-3} - 1000) and (c,d) meridional velocity (m s^{-1}) at (a,c) Day 24 and (b,d) Day 50.	48
5	Time-averaged standard deviation fields of the single ensemble member #11 vs. longitude and latitude. (a) surface density (kg m^{-3} - 1000), (b) SSH (m), (c) vector velocity (m s^{-1}), and (d) surface current speed (m s^{-1}). The 100-, 200-, 500-, 1000-, and 2000-m topographic contours are shown (thin lines). . .	49

6	Surface velocity vectors and speed at (a) Day 21, before separation, and (b) Day 30, after separation, for ensemble member #11. (c) Hovmuller diagram of surface current speed (m s^{-1}) vs. time (days) at Latitude 43.51°N for ensemble member #11. In (c), the longitudes of the 100-, 200-, 500-, 1000-, and 2000-m topographic contours are shown (white thin lines).	50
7	Temporal and ensemble averaged mean fields of the ensemble vs. longitude and latitude. (a) surface density (kg m^{-3} - 1000), (b) SSH (m), (c) surface vector-averaged velocity magnitude (m s^{-1}), and (d) surface current speed (m s^{-1}). The 100-, 200-, 500-, 1000-, and 2000-m topographic contours are shown (thin lines).	51
8	Ensemble spread vs. time (days). Dimensionless N_3 (thick solid line), N_2 (thin solid), and N_h norm (thick dashed solid). Time-integrated wind stress (N m^{-2} day) is also shown (thin dashed line) on left y-axis, and the forecast experiment intervals are indicated (thick horizontal line segments).	52
9	Ensemble standard deviations of surface fields for surface density (kg m^{-3} - 1000) at Day 16.5 (a), 24 (b), and 37 (c), SSH at Day 37 (d; m) and magnitude of surface vector velocity at Day 37 (e; m s^{-1}) vs. longitude and latitude. The 100-, 200-, 500-, 1000-, and 2000-m topographic contours are shown (white thin lines).	53

10	Simulated forecasts at Day 27 for surface density (upper panels; kg m^{-3} - 1000), SSH (middle; m), and magnitude of surface vector velocity (lower; m s^{-1}) vs. longitude and latitude, with initialization on Day 24. Forecast states are shown for the true solution (left panels), persistence (center left), control (center right), and ensemble mean (right). The 100-, 200-, 500-, 1000-, and 2000-m topographic contours are shown (white thin lines).	54
11	Absolute difference fields between the true and forecast solutions of persistence (upper) and control (lower) at Day 27 for surface density (left panels; kg m^{-3} - 1000), SSH (center; m), and magnitude of surface vector velocity difference (right; m s^{-1}) vs. longitude and latitude, with initialization on Day 24. The 100-, 200-, 500-, 1000-, and 2000-m topographic contours are shown (black thin lines).	55
12	Cross-sections at Day 27 and Longitude -124.7°W vs. latitude and depth for density (kg m^{-3} - 1000), for the true solution (a), and the absolute difference fields from the the persistence (b) and control (c) forecasts initialized on Day 24.	56
13	Volume-averaged root-mean-square error in density (a-c; kg m^{-3} - 1000) and vector velocity (d-f; m s^{-1}) for the persistence (thick solid line), control (dashed), and ensemble-mean (thin solid) forecasts vs. time (days) for the (a,d) first, (b,e) second, and (c,f) third forecast intervals.	57

14	Dimensionless N_3 norm of the difference from the true solution for the climatology (dotted line), persistence (thick solid line), control (dashed), and ensemble-mean (thin solid) forecasts, and dimensionless ensemble spread N_3^{ens} relative to the ensemble mean (dashed-dotted) vs. time (days) for the (a) first, (b) second, and (c) third forecast intervals.	58
15	Anomaly correlation coefficient C_{ac} for density (a-c) and vector velocity (d-f) for the persistence (thick solid line), control (dashed), and ensemble-mean (thin solid) forecasts vs. time (days) for the (a,d) first, (b,e) second, and (c,f) third forecast intervals. The nominal value $C_{ac} = 0.6$ for useful skill is indicated (dotted line).	59
16	Ensemble-based forecast relative entropy \mathcal{R}_f (thin solid line) for dimensionless density (a-c) and dimensionless vector velocity (d-f) vs. time (days) for the (a,d) first, (b,e) second, and (c,f) third forecast intervals. The signal (thick solid) and dispersion (dashed) components of \mathcal{R}_f are also shown.	60
17	Predictability statistics for the topography-normal velocity u_h vs. time: (a-c) Volume-averaged root-mean-square error, (d-f) anomaly correlation coefficient C_{ac} , and (g-i) forecast relative entropy \mathcal{R}_f . Values are shown for persistence (thick solid lines), control (dashed), and ensemble-mean (thin solid) in (a-f), and for the signal (thick solid lines), dispersion (dashed), and total forecast relative entropy \mathcal{R}_f (thin solid) for (g-i).	61

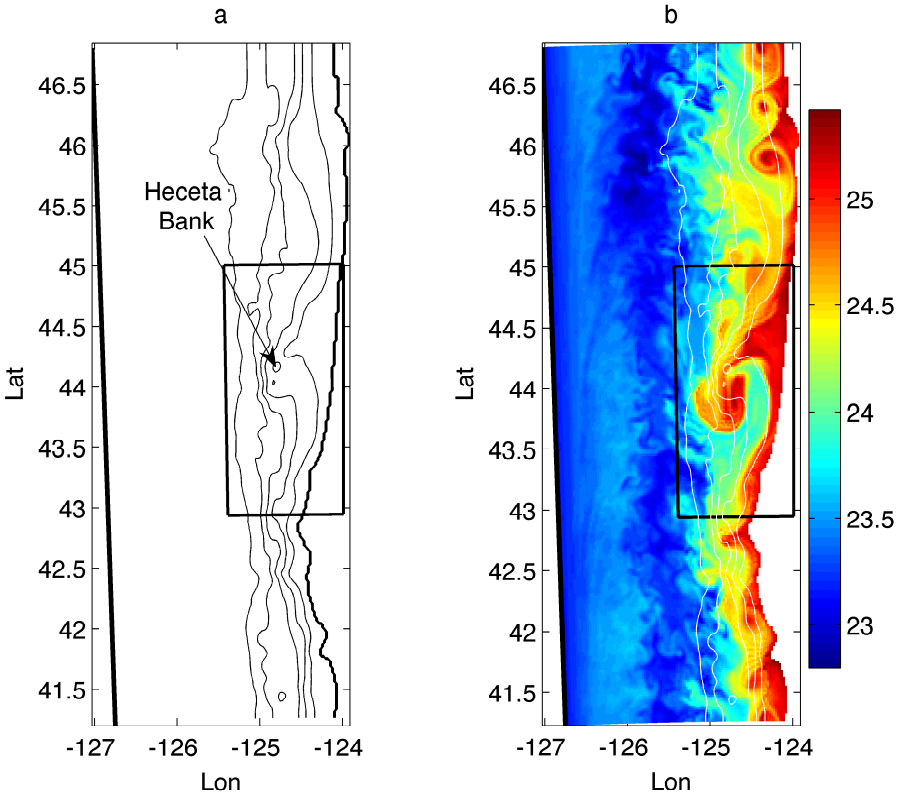


FIG. 1. Model domain vs. longitude and latitude. The inner rectangle indicates the Heceta Bank region, in which ensemble and forecast skill statistics are calculated. (a) Topographic contours (0-, 100-, 200-, 500-, 1000-, and 2000-m contours; thin solid lines; 0 m, thick solid) (b) Surface density (kg m^{-3} - 1000) at Day 16.5 for the single ensemble member #11.

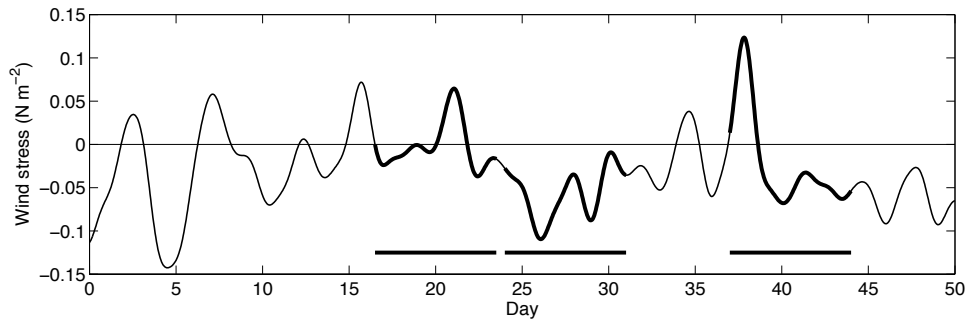


FIG. 2. Alongshore component of buoy wind stress (N m^{-2}) vs time (days). The three forecast experiment intervals are indicated (horizontal line segments).

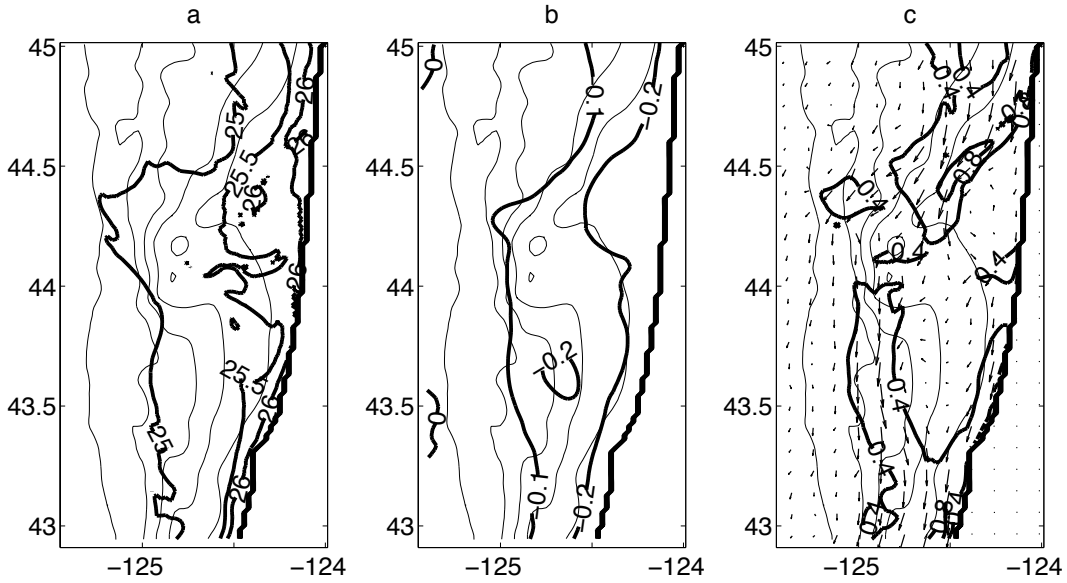


FIG. 3. Surface fields of the single ensemble member #11 at Day 50 vs. longitude and latitude. (a) Density (kg m^{-3} - 1000), (b) SSH (m), and (c) vector velocity and contours of speed (m s^{-1}). The 100-, 200-, 500-, 1000-, and 2000-m topographic contours are shown (thin lines).

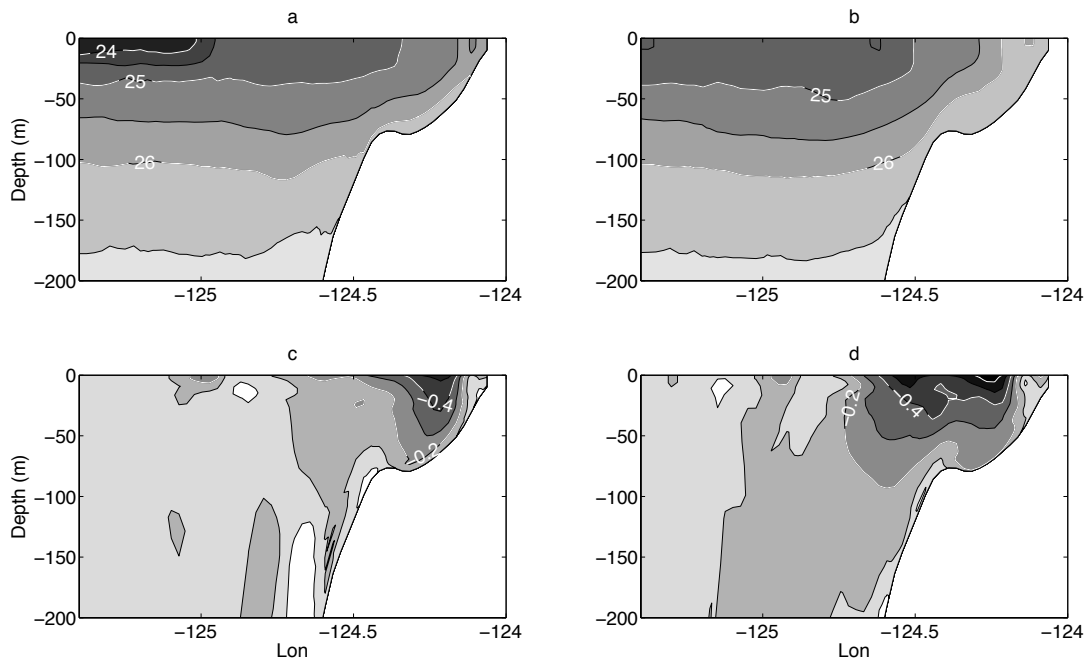


FIG. 4. Cross-sections vs. longitude and depth at Latitude 44.6°N from the single ensemble member #11. (a,b) Density (kg m^{-3} - 1000) and (c,d) meridional velocity (m s^{-1}) at (a,c) Day 24 and (b,d) Day 50.

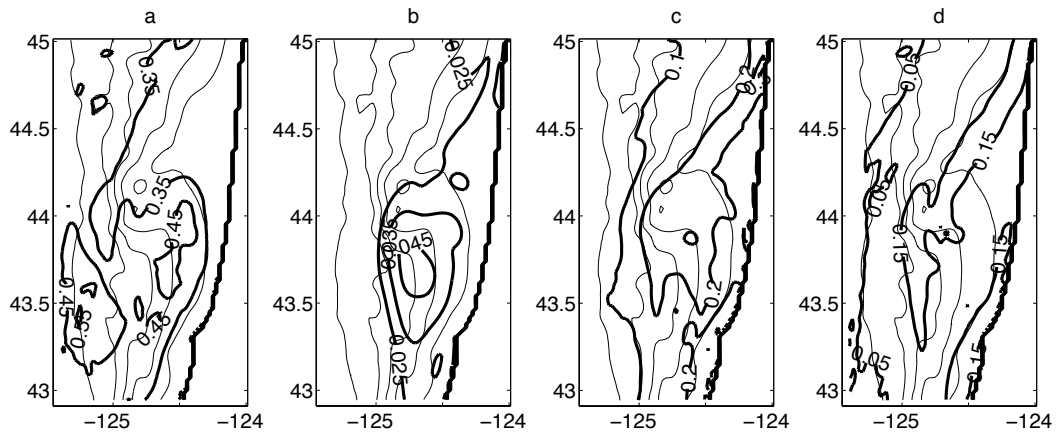


FIG. 5. Time-averaged standard deviation fields of the single ensemble member #11 vs. longitude and latitude. (a) surface density (kg m^{-3} - 1000), (b) SSH (m), (c) vector velocity (m s^{-1}), and (d) surface current speed (m s^{-1}). The 100-, 200-, 500-, 1000-, and 2000-m topographic contours are shown (thin lines).

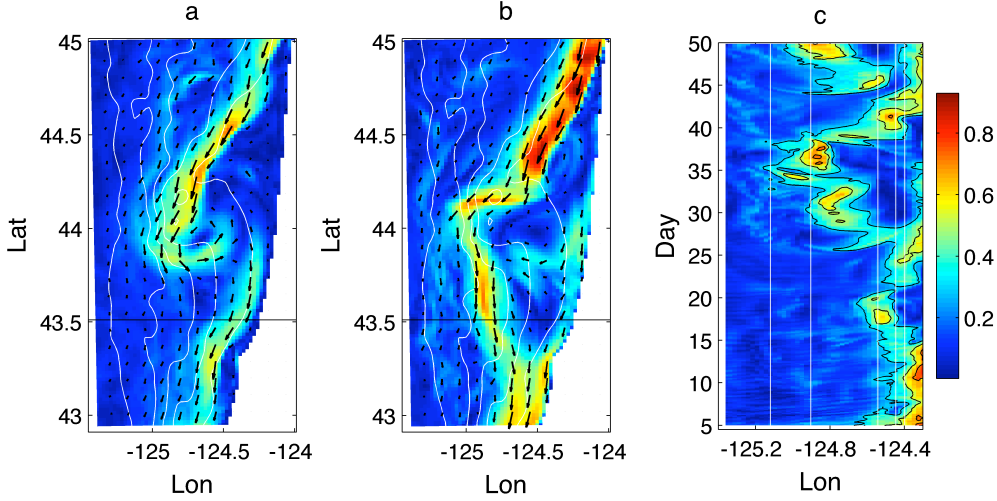


FIG. 6. Surface velocity vectors and speed at (a) Day 21, before separation, and (b) Day 30, after separation, for ensemble member #11. (c) Hovmuller diagram of surface current speed (m s^{-1}) vs. time (days) at Latitude 43.51°N for ensemble member #11. In (c), the longitudes of the 100-, 200-, 500-, 1000-, and 2000-m topographic contours are shown (white thin lines).

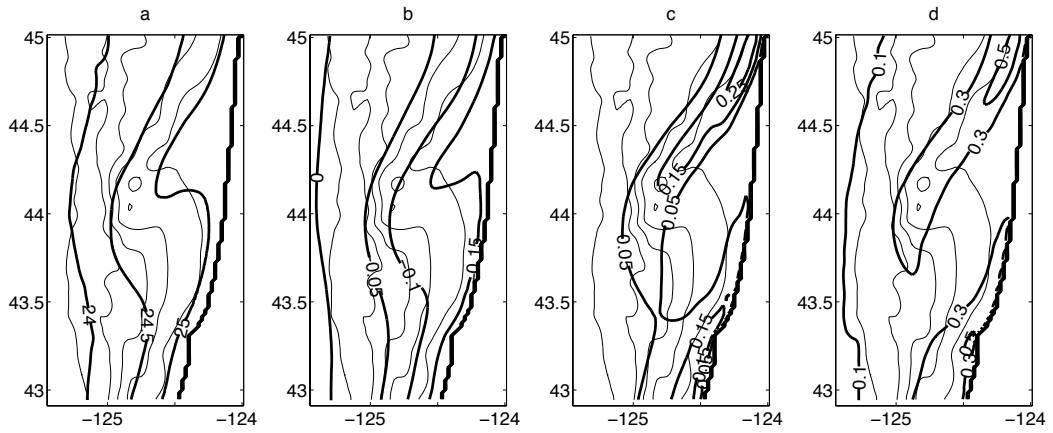


FIG. 7. Temporal and ensemble averaged mean fields of the ensemble vs. longitude and latitude. (a) surface density (kg m^{-3} - 1000), (b) SSH (m), (c) surface vector-averaged velocity magnitude (m s^{-1}), and (d) surface current speed (m s^{-1}). The 100-, 200-, 500-, 1000-, and 2000-m topographic contours are shown (thin lines).

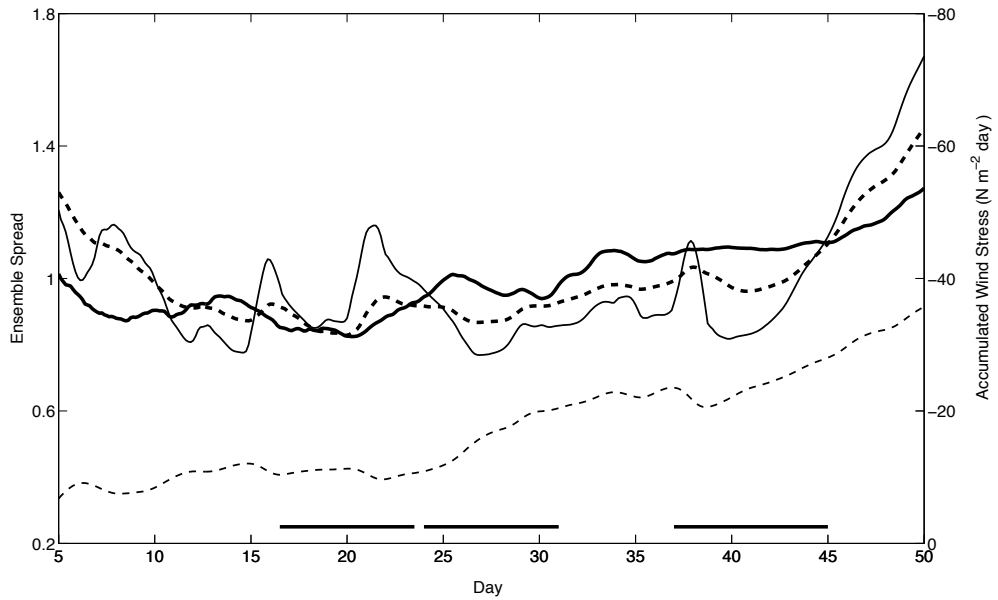


FIG. 8. Ensemble spread vs. time (days). Dimensionless N_3 (thick solid line), N_2 (thin solid), and N_h norm (thick dashed solid). Time-integrated wind stress (N m^{-2} day) is also shown (thin dashed line) on left y-axis, and the forecast experiment intervals are indicated (thick horizontal line segments).

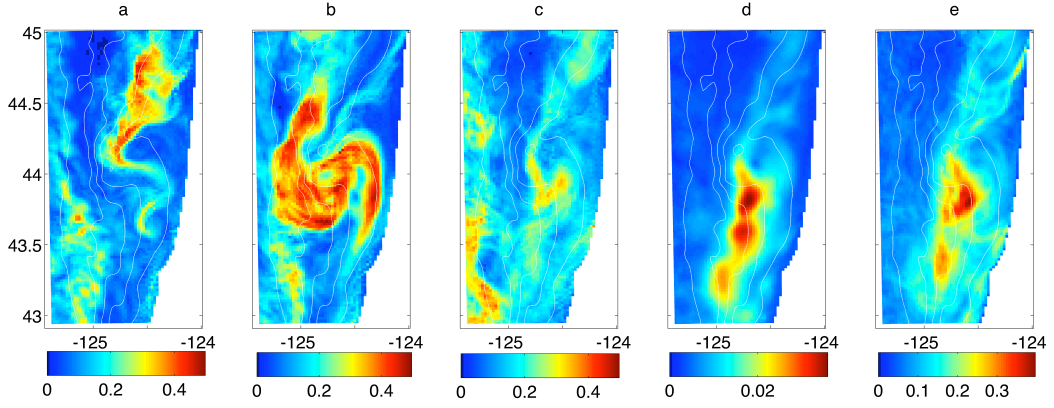


FIG. 9. Ensemble standard deviations of surface fields for surface density (kg m^{-3} - 1000) at Day 16.5 (a), 24 (b), and 37 (c), SSH at Day 37 (d; m) and magnitude of surface vector velocity at Day 37 (e; m s^{-1}) vs. longitude and latitude. The 100-, 200-, 500-, 1000-, and 2000-m topographic contours are shown (white thin lines).

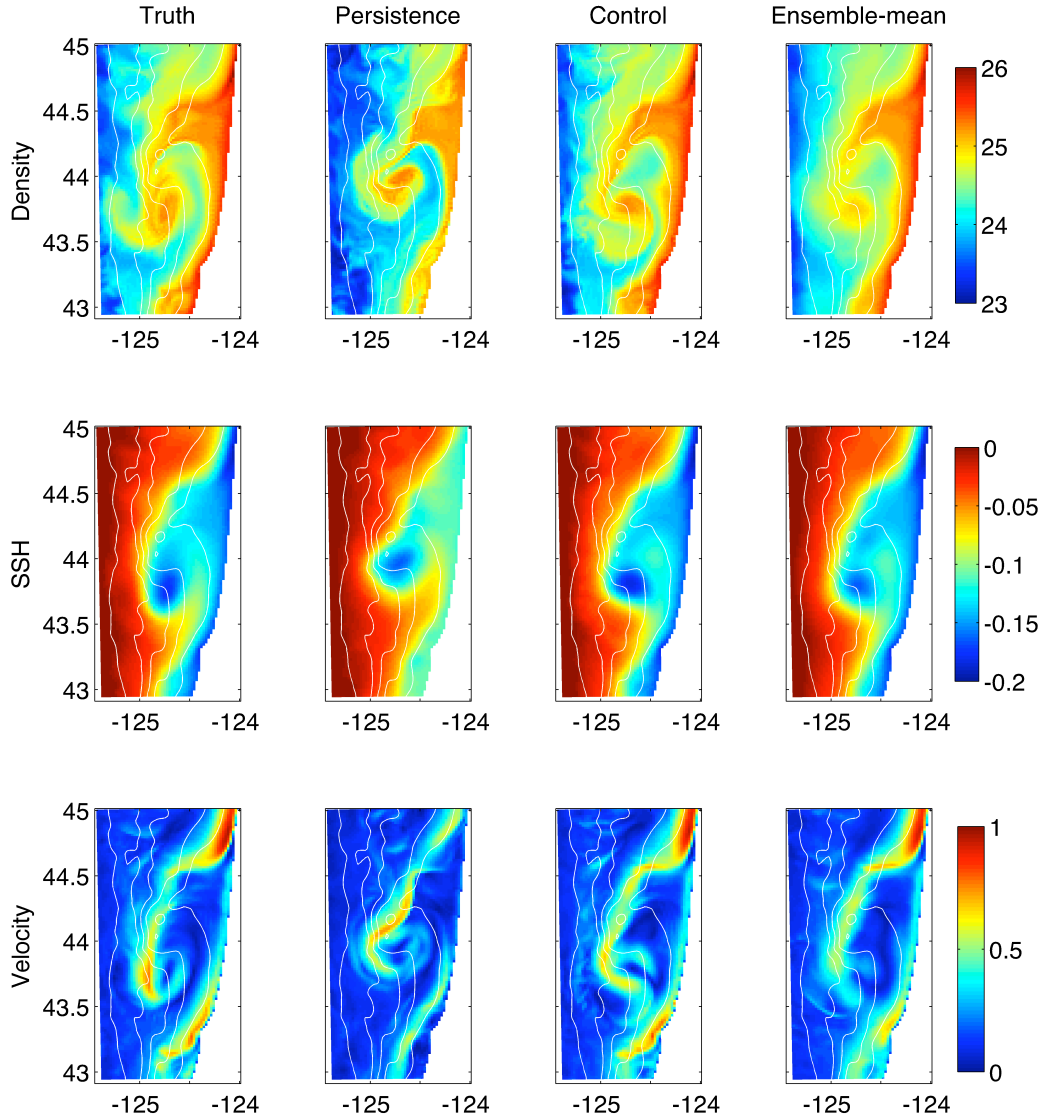


FIG. 10. Simulated forecasts at Day 27 for surface density (upper panels; kg m^{-3} - 1000), SSH (middle; m), and magnitude of surface vector velocity (lower; m s^{-1}) vs. longitude and latitude, with initialization on Day 24. Forecast states are shown for the true solution (left panels), persistence (center left), control (center right), and ensemble mean (right). The 100-, 200-, 500-, 1000-, and 2000-m topographic contours are shown (white thin lines).

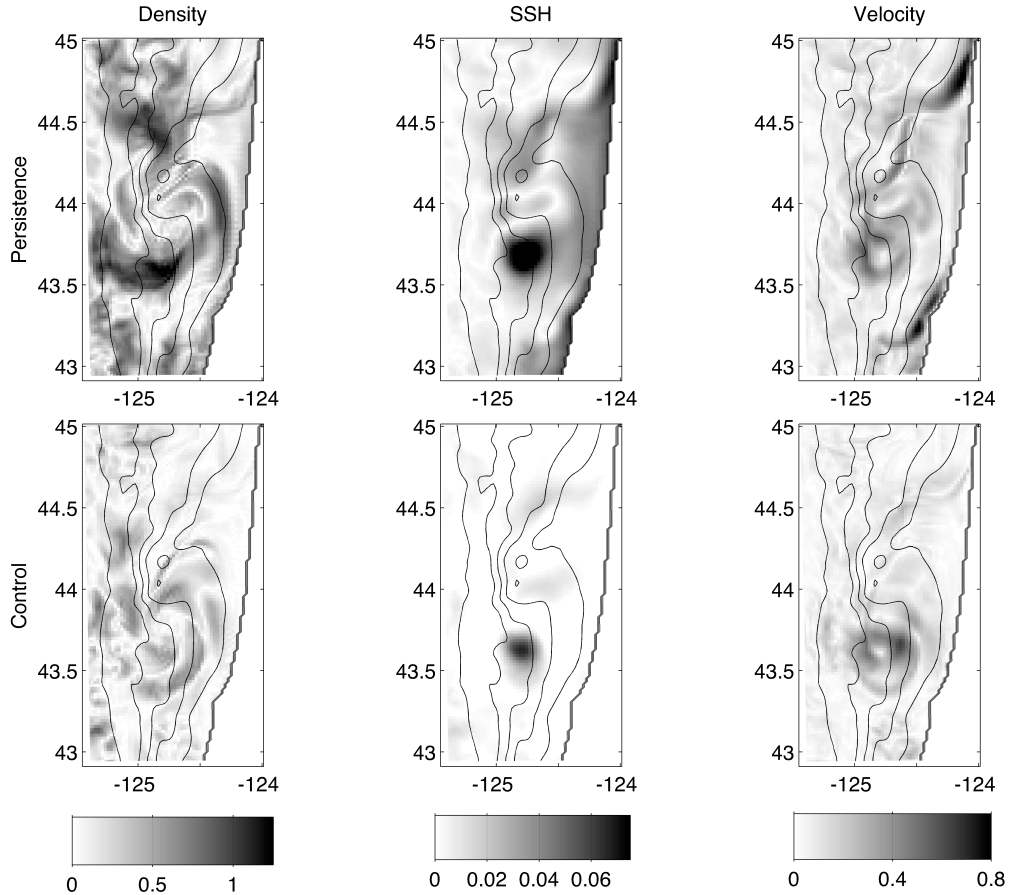


FIG. 11. Absolute difference fields between the true and forecast solutions of persistence (upper) and control (lower) at Day 27 for surface density (left panels; kg m^{-3} - 1000), SSH (center; m), and magnitude of surface vector velocity difference (right; m s^{-1}) vs. longitude and latitude, with initialization on Day 24. The 100-, 200-, 500-, 1000-, and 2000-m topographic contours are shown (black thin lines).

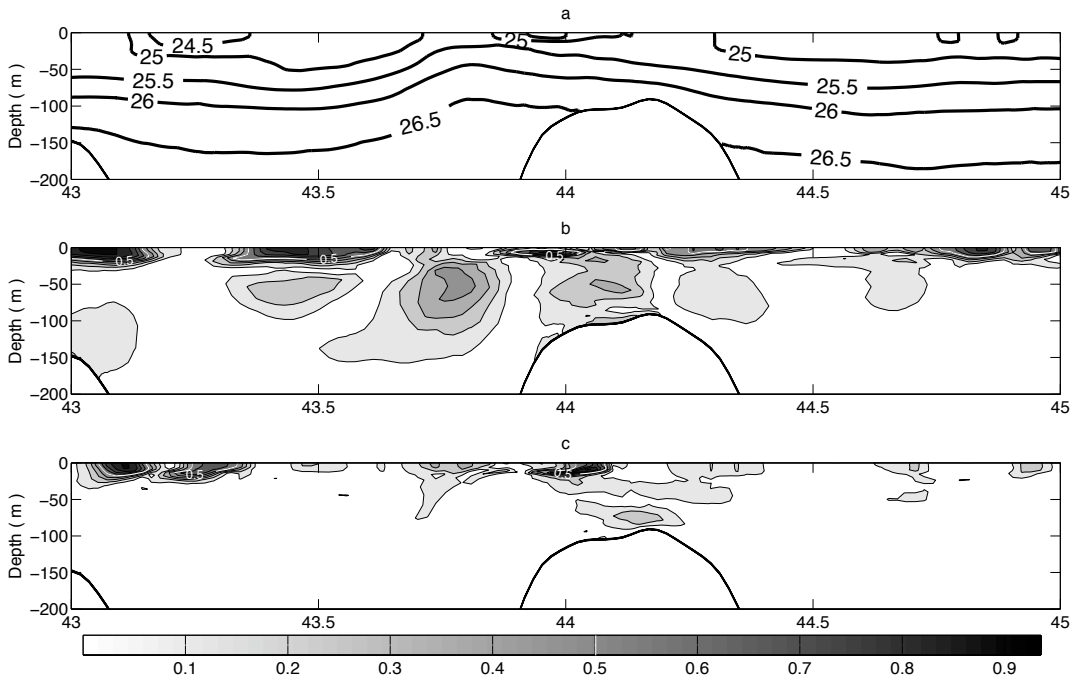


FIG. 12. Cross-sections at Day 27 and Longitude -124.7°W vs. latitude and depth for density ($\text{kg m}^{-3} - 1000$), for the true solution (a), and the absolute difference fields from the persistence (b) and control (c) forecasts initialized on Day 24.

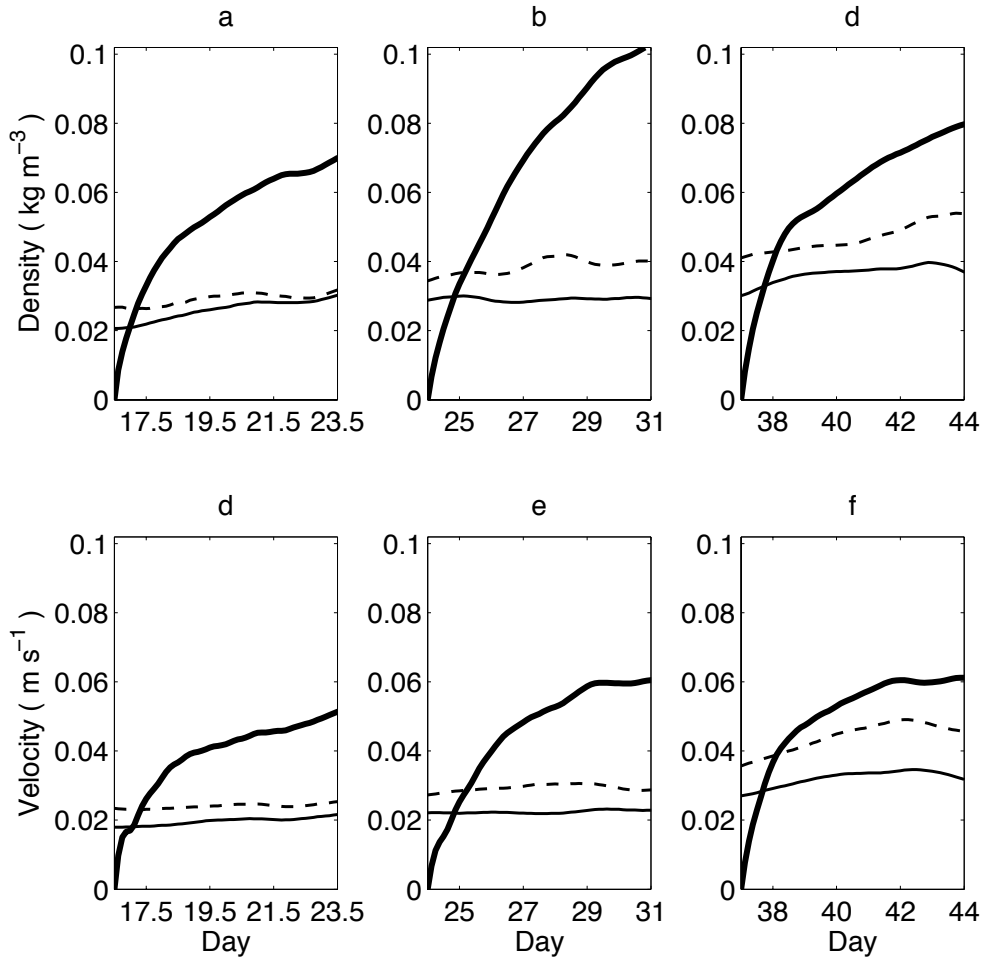


FIG. 13. Volume-averaged root-mean-square error in density (a-c; kg m^{-3} - 1000) and vector velocity (d-f; m s^{-1}) for the persistence (thick solid line), control (dashed), and ensemble-mean (thin solid) forecasts vs. time (days) for the (a,d) first, (b,e) second, and (c,f) third forecast intervals.

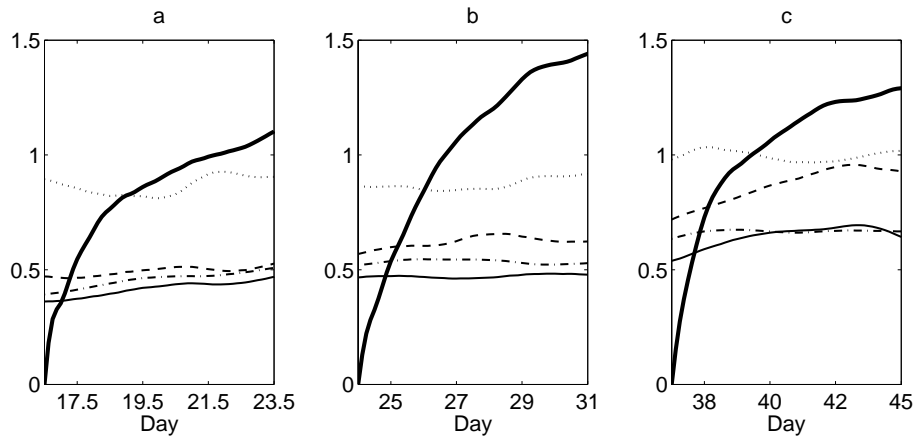


FIG. 14. Dimensionless N_3 norm of the difference from the true solution for the climatology (dotted line), persistence (thick solid line), control (dashed), and ensemble-mean (thin solid) forecasts, and dimensionless ensemble spread N_3^{ens} relative to the ensemble mean (dashed-dotted) vs. time (days) for the (a) first, (b) second, and (c) third forecast intervals.

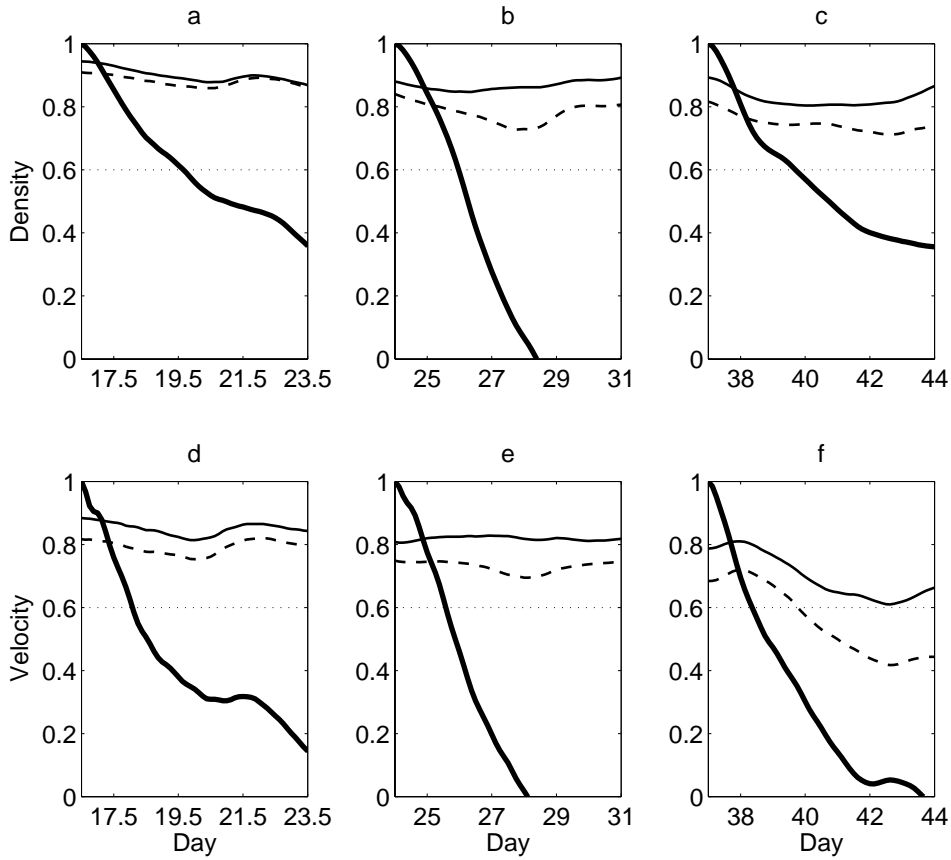


FIG. 15. Anomaly correlation coefficient C_{ac} for density (a-c) and vector velocity (d-f) for the persistence (thick solid line), control (dashed), and ensemble-mean (thin solid) forecasts vs. time (days) for the (a,d) first, (b,e) second, and (c,f) third forecast intervals. The nominal value $C_{ac} = 0.6$ for useful skill is indicated (dotted line).

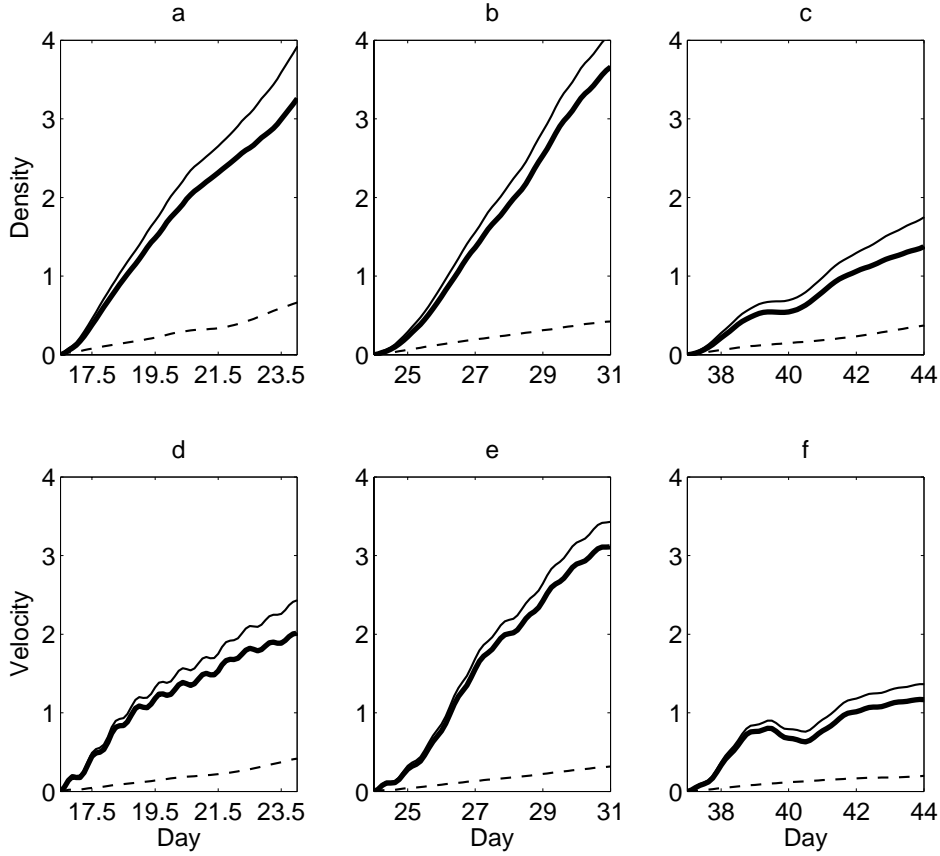


FIG. 16. Ensemble-based forecast relative entropy \mathcal{R}_f (thin solid line) for dimensionless density (a-c) and dimensionless vector velocity (d-f) vs. time (days) for the (a,d) first, (b,e) second, and (c,f) third forecast intervals. The signal (thick solid) and dispersion (dashed) components of \mathcal{R}_f are also shown.

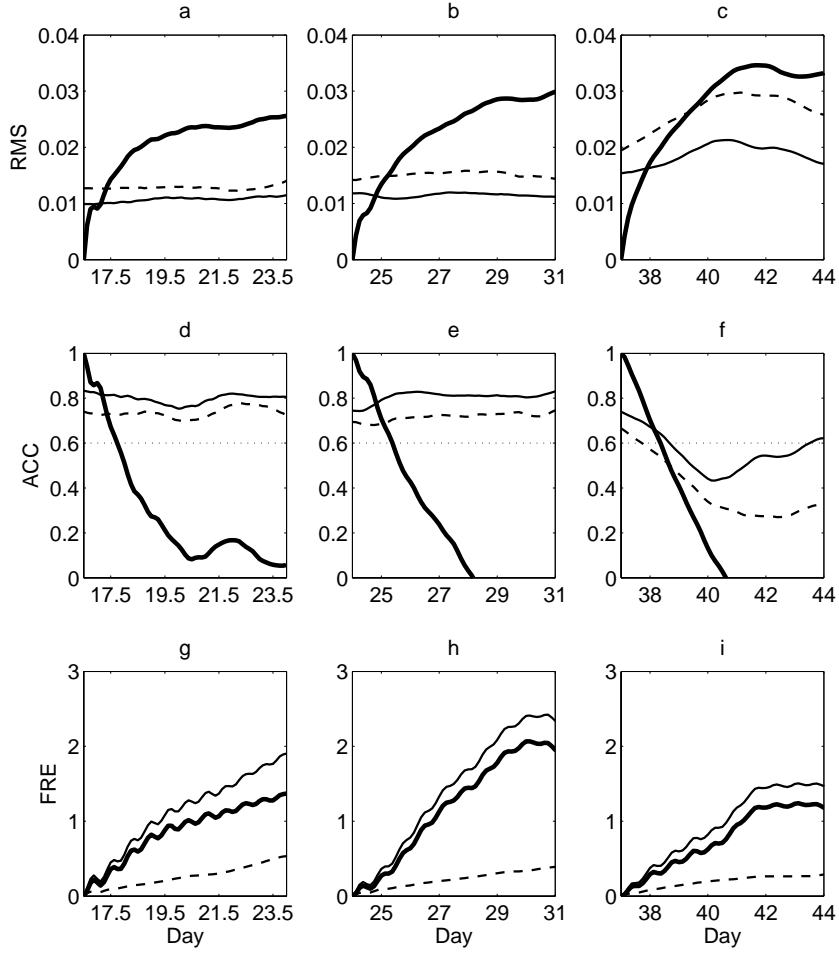


FIG. 17. Predictability statistics for the topography-normal velocity u_h vs. time: (a-c) Volume-averaged root-mean-square error, (d-f) anomaly correlation coefficient C_{ac} , and (g-i) forecast relative entropy \mathcal{R}_f . Values are shown for persistence (thick solid lines), control (dashed), and ensemble-mean (thin solid) in (a-f), and for the signal (thick solid lines), dispersion (dashed), and total forecast relative entropy \mathcal{R}_f (thin solid) for (g-i).

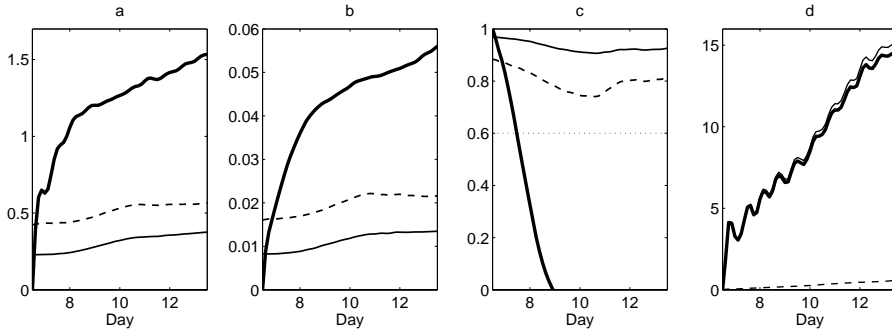


FIG. 18. Predictability statistics: (a) N_3 norm (b) volume-averaged root-mean-square error density, (c) volume-averaged anomaly correlation coefficient C_{ac} for density (d) forecast relative entropy \mathcal{R}_f for density. Values are shown for persistence (thick solid lines), control (dashed), and ensemble-mean (thin solid) in (a-c), and for the signal (thick solid lines), dispersion (dashed), and total forecast relative entropy (thin solid) for (d).

List of Tables

1	Spatial averages in order on days 19.5, 27, and 40 of the absolute difference from truth for climatology, persistence, control and ensemble mean forecast fields	64
---	--	----

TABLE 1. Spatial averages in order on days 19.5, 27, and 40 of the absolute difference from truth for climatology, persistence, control and ensemble mean forecast fields.

	Surface density (kg m^{-3})			SSH (m)			Surface current (m s^{-1})		
Climatology	0.299	0.221	0.231	0.0160	0.0097	0.011	0.079	0.089	0.082
Persistence	0.212	0.379	0.192	0.0076	0.0176	0.012	0.073	0.103	0.111
Control	0.138	0.158	0.147	0.0030	0.0053	0.008	0.043	0.058	0.070
Ensemble Mean	0.125	0.143	0.119	0.0029	0.0048	0.007	0.038	0.050	0.054